MACQUARIE UNIVERSITY

Amphibole and Magma Evolution: Insights from composite xenoliths from Batan Island, Philippines

Mitchell Gerdes

Masters of Research Thesis

10/10/2016

Department of Earth and Planetary Sciences

Faculty of Science and Engineering

Macquarie University, North Ryde, Australia

MACQUARIE
University

Statement of Originality

The work presented here is all my own work, and has not been reproduced elsewhere, submitted to another university, or institution, unless acknowledged.

Signed: Dated: 10-10-16

Mitchell Gerdes

Table of Contents

Acknowledgements v

Abstract 1

1. Introduction 2

2. Literature Review 3

2.1. Arc Settings and Mantle Xenoliths 3

2.2. Stories within Mantle Xenoliths 5

2.2.1. Geochemical trends in arc xenoliths 5

2.2.2. Petrographic variations in arc xenoliths 6

2.2.3. Modelled processes causing change in arc xenoliths 7

2.3. Batan Island, A Natural Laboratory 9

3. Aims of Study 11

4. Methods 12

4.1. Petrographic analysis 12

4.2. Elemental analysis 12

4.3. Dingo- Neutron Tomography 13

5. Results 14

5.1. General sample description and Neutron Tomography 14

5.2. Petrography and quantitative spatial analysis 14

5.2.1. Peridotite fragments. 14

5.2.2. Hornblendite rind and melt-rock reaction. 17

5.2.3. Hornblende Gabbro 20

5.3. Composite Xenolith- Mineral chemistry 22

5.3.1. Major element concentrations 22

5.3.2. Trace element abundances 25

5.4. Host Lava 28

5.4.1. Host Lava- petrography 28

5.4.2. Host Lava- major element chemistry 30

6. Interpretation 31

6.1. Significance of textural relationships in the xenolith 31

6.1.1. Stage 1- Deformed harzburgite. 31

6.1.2. Stage 2- The reaction assemblage 31

6.1.3. Stage 3- The hornblende gabbro. 32
6.2.4. Stage 4- Host magma 33
6.2.5. Petrographic interpretation. 34
6.2. Geothermometry- further constraining physical conditions of origin 34
6.2.1. P-T constraints for the peridotite fragments 34
6.2.2. P-T conditions for the hornblendite rind. 35
6.2.3. P-T constraints for the hornblende gabbro 36
6.2.4. P-T constrains for the host lava. 36
6.2.5. P-T interpretation. 36
6.3. Insights from trace element data 38
6.3.1. Chemical evidence for nature and origin of the harzburgite fragments. 38
6.3.2. Linking the reaction assemblage to the hornblende gabbro. 38
6.3.3. The link between olivine, equilibrium melt, and host andesite. 39
6.3.4. Trace element interpretation. 40
7. Petrogenic Model: Combining petrographic and geochemical interpretations 40
7.1. Xenolith Formation 40
7.2. Amphibole fractionation in arc settings 43
7.3. Batan Island volcanism 44
8. Conclusions 45
References 46
Appendix 1 51
Appendix 2 52
Appendix 3 58

Acknowledgements

The past year has been intense to say the least. I've learnt much more that I thought I would, and as a weird spin on it all, it's humbling to learn how much I still have to learn (and of course there is to find out) about the discipline. This year has in no way been solitary, and I would like to thank the following people- not because it's convention, but because these people have made the year worth its while.

To my supervisors, Simon Turner and Sandra Piazolo, a whole-hearted thank you for sticking with me, for having the patience and making the time to sit down and work through problems I've had. Thank you for letting me tackle an interesting project with an incredibly unique and beautiful rock sample. And lastly, somehow you have been on the end of emails throughout the entire year - without fail - with edits, suggestions and the occasional nudge to hurry up! The support from you both has been fantastic. Thank you.

To John Adam, I need to thank you for the meetings going through geochemical datasets, arm waving discussions, especially since there were times you came in at my convenience. It is greatly appreciated.

To Joseph Bevitt and Floriana Salvemini at ANSTO (Australian Nuclear Science and Technology Organization) a big, big, big thank you for finding time to run the xenolith through Dingo, and then to find time in your busy schedules to show me around the facility, explaining how the technique works. That was an awesome day- I'm not going to forget that nuclear dinosaur joke either, Joseph.

There are several people who also went out their way to help me with the analytical techniques. Your help has not gone unacknowledged! Thank you to those from Macquarie University: Rosanna Murphy, Cait Stuart Sarah Gain, Dave Adams, Norman Pearson and Nathan Daczko for help with the analyses in the GAU (Geochemical Analytical Unit). Thank you Alex Stokes for access, and help with, the work completed at the Macquarie University branch of Optofab in the Australian National Fabrication Facility.

To Jen Rowland – OK so you might turn around and say it's part of your job, BUT – the few coffee meetings got me back on track, and full of confidence. I hope to keep running into you up at the pool!

To the other Masters students in the hut – ice box – sweat box – tin box – office – permanent-looking demountables, thanks for the company. Whilst there are too many to name you individually, a special thanks to Anthony Finn and Carla Raymond for the countless gym sessions, coffee sessions, lunch sessions…the list goes on. I wish you all the very best of luck with your theses in the coming 12 months. It's a hard slog… but "Maximum effort…" right? If there is ever a need to yell, complain, question, argue, arm wave or have a coffee, I am always on the end of a call.

To the squad I coach. Coaching you muppets was probably the single most head clearing event of each day. You had to deal with the moods, the odd sessions, the yells… but every session cleared the thick red mist in front of my face and kept me going. A big thank you. Legends.

Lastly, definitely the biggest thank you to my family. This year could not have been done without you. The voices of reason and the ears that listened. Lachlan, head down and smash the HSC- we are both free men soon!

Abstract

Volcanism is the end product of many complex processes occurring beneath volcanic arcs at subduction settings. Processes, such as metasomatism of the mantle, partial melting, crystal fractionation and eruption, can only be inferred from erupted material. Two exceptions are arc terranes and the rare entrainment of mantle xenoliths. Multiple component xenoliths have been erupted in high K, calc-alkaline andesites on Batan Island, the Philippines. However literature has only described the peridotite components, not the amphibole rind or gabbro components. Combining novel and conventional analysis techniques, prior work has been placed in the context of this composite xenoliths formation. Interestingly, amphibole is a major mineral phase in the all xenolith components, but non-existent in the host lava. Recent literature uses trace element abundance in lavas to infer that amphibole fractionation occurs at many arc settings, yet no physical evidence saw the process occurring (e.g. Davidson et al., 2007). This composite xenolith shows amphibole forming under both reaction and cumulate conditions, two processes which amphibole may evolve a magma in arc settings. As such, the evidence shown can be used as a novel analogue to processes occurring in other arc settings.

Davidson J., Turner S., Handley H., Macpherson C. and Dosseto A., (2007), Amphibole "sponge" in arc crust?, *Geology*, 35(9): 787-790.

1. Introduction

Volcanic arc settings not only produce some of Earth's most compositionally diverse magmatism and volcanic hazards, they are an important site for crustal destruction and continental regrowth (Rudnick, 1995; Dessimoz et al., 2012). The type of volcanism is a direct result of an evolving mantle wedge and, thus, the suite of natural hazards affecting communities related to volcanic type will change with time. For example, basaltic scoria cones (e.g., Tanna Island, Vanuatu) cause flood basalts and are relatively benign. With time, the basalt produces fertile soils.

Andesitic stratovolcanoes (e.g., the Megata region of Japan) pose differing threats and are the result of more evolved magmas. Lahars, lava flows, landslides and ash clouds have the potential to cause major disruptions. Rhyolitic calderas (e.g., Lake Taupo, New Zealand) are the result of highly siliceous magmas. They produce the most catastrophic destruction when pressures in the magma chamber are suddenly released. These three different locations are the same tectonic setting producing very different volcanism.

Arc volcanism is the end product of many complex processes including, but not limited to, metasomatism of the mantle by the subducting plate, partial melting, crystal fractionation and eruption. Unfortunately, only the very last process can be directly observed leaving the rest to be inferred from lava chemistry. One exception to this hindrance is the rare (e.g., Nixon, 1987) entrainment of mantle xenoliths that offer direct sampling of the deeper, sub-volcanic regions. These have often been inferred to represent analogues of the arc magma source region and hence afford unique insights into the nature of the mantle peridotite (e.g. fertile versus depleted) and the composition and nature of metasomatic components added to this peridotite (e.g. aqueous fluids, sediment melts or supercritical fluids).

Hydrous minerals, such as amphibole, are common mineral phases in arc xenoliths and usually occur as cross cutting veins (e.g. Bénard and Ionov, 2013). Whilst common in crustal nodules found in arc lavas (e.g. Arculus and Wills, 1980), amphibole is surprisingly rare as a phenocryst phase in arc lavas. In this regard, there has been much recent debate surrounding the seemingly enigmatic role played by amphibole in arc lava petrogenesis (Anderson, 1980; Davidson et al., 2007; Ridolfi et al, 2010; Neal, 1988). Nevertheless, Davidson et al. (2007, 2013) have used rare earth element data to argue for an important role for amphibole in arc lava petrogenesis and suggested that this mineral may provide a sink for H_2O in arc crust. Accordingly, the role amphibole plays in arc settings has been termed cryptic (Davidson et al., 2007; Smith, 2014) due to the lack of physical evidence showing a process that crystallizes amphibole.

Batan Island, Philippines, is one of the well-known localities where composite mantle xenoliths have been entrained in ascending magmas and erupted at the surface. Composite xenoliths entrained in high K, calc-alkaline andesitic lavas on Batan Island (Sajona et al., 2000) have amphibole in all three components; peridotite nodule, amphibole rind and amphibole gabbro. Geochemical studies of the peridotite nodules demonstrates that metasomatism of the mantle beneath Batan was not only recent (e.g. Turner et al., 2012), but was derived from subducted slab and sediment fluids giving the setting the unique, 'arc-like' signature (Maury et al., 1992; Schiano et al., 1995; Turner et al., 2012; Fourcade et al., 1994; Sajona et al., 2000; Vidal et al., 1989). Further petrographic studies of the peridotite nodules show grainsize variation and the loss of a melt fraction (Arai et al., 1996; Aria and Kida, 2000; Arai et al., 2004).

Much of the literature has focused on the peridotite nodules, and only select studies have mentioned the amphibolite rind and amphibole gabbro (Arai and Kida, 2000; Arai et al., 2004). Accordingly, the full context behind formation of these composite xenoliths has not been adequately addressed. For example, whilst the peridotite has a clear mantle origin, it is less clear whether the composite nature of the xenolith is derived from processes occurring within the mantle wedge or the sub-arc lithosphere. Under what conditions did the amphibolite and gabbroic rinds form? What, if any, is the relationship of the latter to the host lava? Using a carefully selected and representative xenolith from Batan Island, this thesis aims to address these outstanding questions through a combination of petrographic and geochemical techniques including a novel Neutron Tomography technique. It will establish the full context of the chosen xenolith history and contribute to wider questions surrounding the importance of amphibole in arc settings.

2. Literature Review

2.1. Arc Settings and Mantle Xenoliths

Arc settings are sites of frequent earthquakes and volcanism. They are the result of two converging tectonic plates: one being thrust under the other. The path of subduction can be identified by studying earthquake focal points, the steepness of which not only varying between locations, but also along a single arc (e.g. Yang et al., 1996). This process, 'subduction,' creates a wedge of mantle which is subjected to partial melting caused by released fluids from the hydrated subducting slab. Cold tectonic slabs alters the geotherm and confines the mantle wedge of an arc setting as illustrated in Figure 2.1.

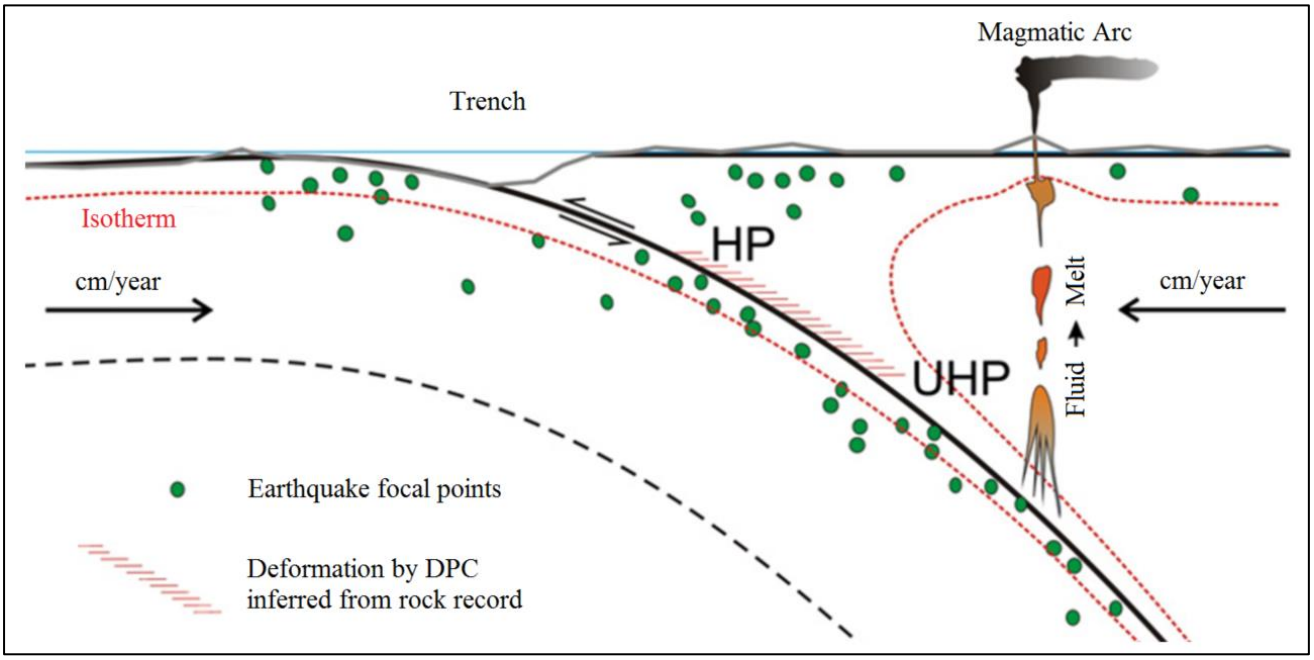

Figure 2.1: Schematic of arc settings and the mantle wedge. After Wassmann and Stöckhert (2013). DPC- Dissolution Precipitation Creep. HP- High Pressure. UHP- Ultra HP.

Modern arc settings are clustered primarily on the western Pacific. For example, Kamchatka in Alaska (e.g. Béneard and Ionov, 2013), the main islands of Japan (e.g. Abe et al., 1998; Takahashi, 1978), throughout the Philippines (e.g. Defant et al., 1990), South Asia through Papua New Guinea (e.g. Mcinnes et al., 2001), and from Samoa through the Tonga-Kermadec Arc to New Zealand (e.g. Neal et al., 1988). Volcanism at these settings is the end result of processes occurring beneath the volcano, within the mantle wedge. However, only eruptions can be directly observed, and so any process occurring beneath the volcano is inferred from analyzing microstructure textures and geochemistry of lavas. There are two exceptions. The first are exhumed arc settings (arc terranes) which can provide valuable insights into the structure of arc settings (e.g. Le Roux et al., 2014; Imon et al., 2004; El-Rahman et al., 2012), however the majority of these arc terranes have been rapidly altered when exhumed. The second is the rare (e.g. Nixon, 1987) inclusion of mantle xenoliths in erupted arc lavas. Mantle xenoliths are a unique opportunity to expand on existing knowledge regarding arc settings and their processes.

2.2. Stories within Mantle Xenoliths

Mantle xenoliths vary in both chemistry and morphology, suggesting alteration prior to eruption. This change is referred to as metasomatism. Accordingly, the xenoliths are described as analogues to the magma source region and processes occurring within the mantle wedge. With this assumption, the chemical and morphological nature of the xenoliths can be directly used to describe processes within the mantle wedge and sub-arc lithosphere. For example, Turner et al. (2012), showed a remarkable correlation between Batan xenoliths and their host lava (Figure 2.2a). Whilst the xenoliths may have been sampled by the ascending magma and not the actual source of that magma, the striking correlation suggests that the magma source and xenoliths may be the same. As such, studies combining both geochemical and petrographic investigations provide the most context surrounding the xenoliths history.

2.2.1. Geochemical trends in xenoliths

Chemical alteration to the mantle with no mineralogical change is defined as cryptic metasomatism. Cryptic metasomatism is easily defined through incompatible trace element analysis. The pattern no longer reflects a depleted or primitive mantle reservoir and are normalized to show the clear deviation from these reservoirs. Figure 2.2b shows how the abundance of trace elements in clinopyroxene from Paua New Guinea xenoliths have deviated from primitive mantle values (normalized value of 1) and the pattern no longer represents a depleted mantle signature (e.g. McDonough and Sun, 1995).

Addition of subducted sediment and hydrated slab to the mantle wedge often results in an enrichment in trace elements not seen in other tectonic settings. Often referred to as an 'arc signature,'

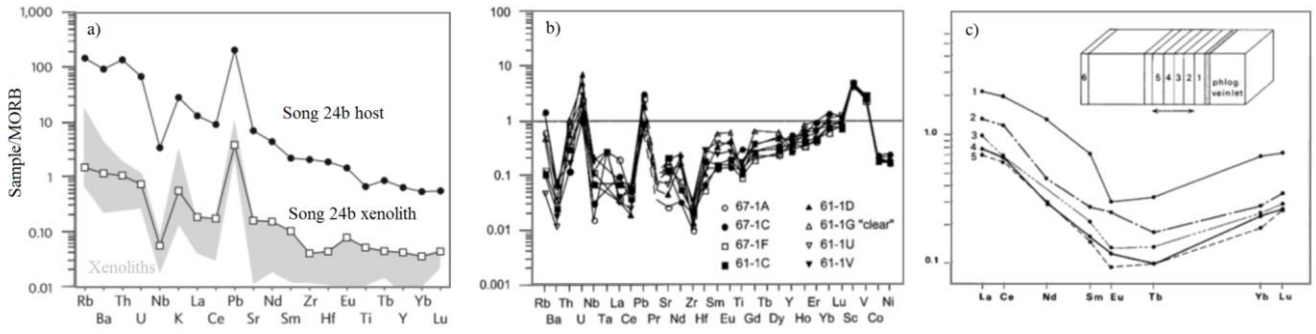

Figure 2.2: A series of trace element plots. a) Incompatible trace element plot comparing xenoliths of host lava, MORB normalized after Turner et al. (2012). b) Incompatible trace element plot of clinopyroxene in xenoliths from Lihir, PNG, normalized to Primitive Mantle after Grégoire et al. (2001). c) REE plot showing a spatial relationship to a phlogopite vein, chondrite normalized after Vidal et al. (1989).

elevated abundances in fluid mobile elements (e.g. Large Ion Lithophile Elements (LILE) such as Sr, Ba, Rb, Th, U, and Pb; and REE's) is defined as a crucial indication of slab derived fluids interactive with the above mantle wedge (e.g. Grégoire et al., 2001; Franz et al., 2002; Prouteau et al., 2001). Similar enrichments in trace elements are noted in arc xenoliths from other arc settings (e.g. South Korea, Choi et al., 2005; Kamchatka, Beneard and Ionov, 2013; Megata Japan, Abe et al., 1998; Solomon Islands, Neal, 1998; Lesser Antilles, Parkinson et al., 2003). In these instances, there is no physical change in this episode of metasomatism.

Changes to chemistry are not only limited to such episodes of cryptic metasomatism. Often, a chemical change is the result of veining. Diffusion of material (Figure 2.2c) demonstrates how proximity to a vein can result in spatial trace element chemistry variation. Whilst the trace element pattern does not change, the abundance of material increases with proximity to the phlogopite veinlet (refer to Vidal et al., 1989). Thus, whilst the chemical nature of the xenolith is important, such studies should always accompany a spatial analysis to provide the fullest context.

2.2.2. Petrographic variations in xenoliths

Physical appearances, from microstructure textures to hand sample morphology, of arc xenoliths are highly variable. For example, crystal plastic deformation induced by a the stress regime, veining and loss of a melt fraction are some common features of arc xenoliths which effect the mantle wedge from small to large scales (e.g. Debari et al., 1987; Ishimaru et al., 2007).

The growth of a new mineral defines a modal metasomatic event. Figure 2.3 shows a variety of microstructures from Kamchatka (Alaska) xenoliths. Two modal metasomatism events are clearly defined by veins '1' and '2' in Figure 2.3a cutting the harzburgite (implied loss of melt fraction). Whilst some veins cut through crystals, others exploit grain boundaries, such as those in Figure 2.3b linking pockets of much finer grains. The vein in Figure 2.3c is the same as in Figure 2.3b. The morphology of the vein also provides valuable information; the exploitation grain defects (e.g. fractures and subgrains) in a non-uniform shape demonstrates how reaction occurs faster along grain defects (e.g. Ortoleva et al., 1987).

Reaction textures are common in arc xenoliths, and whilst simple petrographic light microscopes can identify general features of reaction in thin section, backscatter imagery highlights reaction features more clearly (Figures 2.3d-f). Oftentimes, reactions result in finer grain sizes with 'embayed' features and chemically zoned growth of new mineral (e.g. orthopyroxene in Figure 2.3d). In Figure 2.3e, the secondary

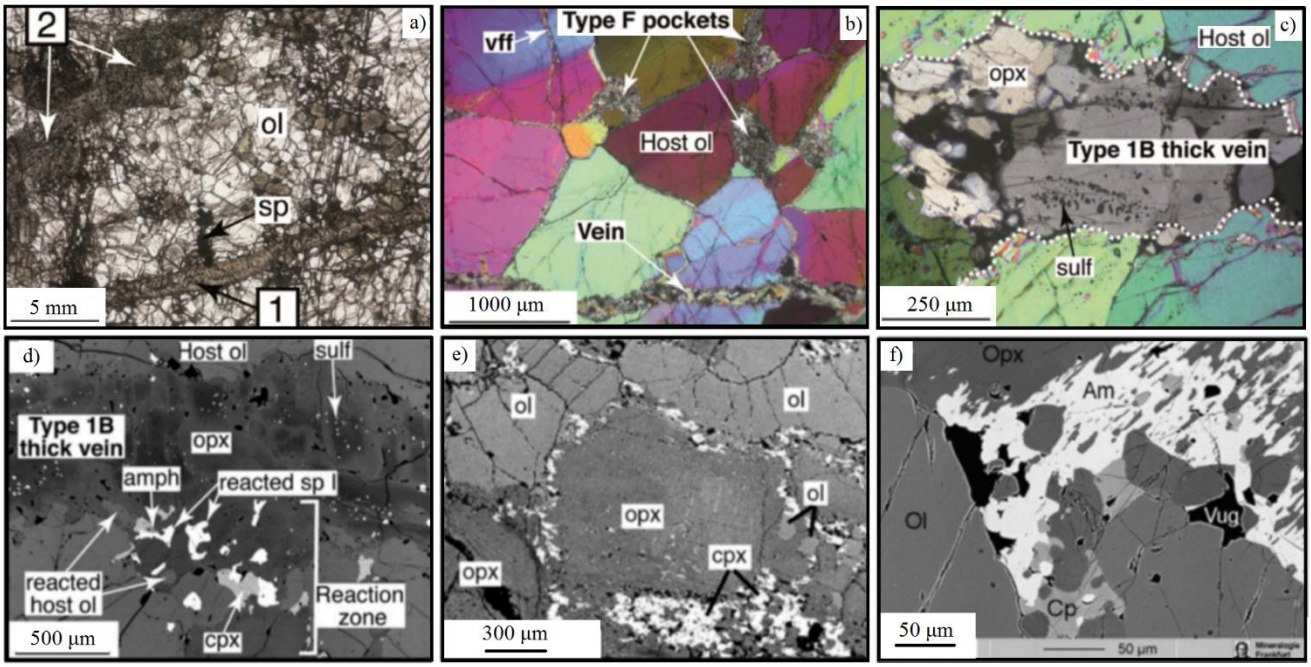

Figure 2.3: Microstructures of Avacha peridotites. a) Plane polarized light (PPL) thin section showing two vein types (refer Bénard and Ionov, 2013), ol-Olivine, sp-Spinel. b-c) Cross polarized light (XPL) images of harzburgite and spatial nature of Type F (fine grained) pockets and orthopyroxene veins after Bénard and Ionov (2013). d-f) Backscatter electron micrographs of reaction features. d) Shows zoned orthopyroxene and embayed, relict spinel and olivine grains in reaction zone from Béneard and Ionov (2013). e) Fluid reacting with orthopyroxene, forming fine grains exploiting grain boundaries after Halama et al. (2009). f) Hydrous mineral- amphibole- with no crystallographic structure or boundary reacting with orthopyroxene, space change has also occurred created vugs from Ionov and Seitz (2008).

mineral is the bright clinopyroxene (cpx) exploiting grain boundaries between orthopyroxene (opx) and olivine (ol). Importantly, on much finer scales, reactions and crystallization of new minerals often results in density and space changes, either forcing host minerals to crack further, or creating voids (vugs, Figure 2.3f). As a result of this variation, nearly every suit of xenoliths provides a different story to be told.

2.2.3. Modelled processes causing change in arc xenoliths

Understanding how metasomatism works is vital in deciphering xenolith formation and the wider scale process. Processes can be directly inferred from the petrographic texture. The mineral textures shown in Figure 2.3d-f are reaction features, caused by a chemical gradient, and the result of reactive instabilities (e.g. Ortoleva et al., 1987; Liang and Guo, 2003). A melt reacts with the host rock, dissolving the host and produces a new mineral and the process continues. The 'moving boundary' problem (e.g. Chadam et al., 1986; Morgan and Liang, 2003) is illustrated in Figure 2.4. The initial dissolution front (2.4a) creates space

which is immediately filled and the reaction continues (2.4b). The process is clearly seen in Figure 2.4c, exploiting grain boundaries and defects where the movement of material is easiest.

Driving mechanisms for reactive instabilities has been debated in literature. Ortoleva et al. (1987) defines chemical diffusion within the melt as a driver for stabilization of the reaction, however, Liang and Guo (2003) show that chemical diffusion in the melt can actually drive dissolution reactions (Figure 2.5). Diffusion across a dissolution front (2.5a), can either promote stabilization of the reaction by moving material across the boundary (2.5b), or promote a continuation of the reaction by moving material into the boundary (2.5c). Assumedly, the compositional difference between melt and wall rock should determine the movement of material and subsequent concentration profile.

Whilst reaction instabilities are chemically driven, the tectonic regime provides and extra variable influencing change to the mantle wedge in arc settings. Commonly referenced in literature is Dissolution Precipitation Creep (DPC). This process requires both chemical and physical stresses to occur. Arc settings satisfy these variables (refer to Wassmann and Stöckhert, 2013) and resulting features are most easily defined in microstructure textures. For example, Figure 2.3d shows the secondary features (orthopyroxene) is zoned under backscatter imagery. Whilst zoning is a chemical feature, stress related microstructures are also pivotal in influencing how such processes take effect.

Converging tectonic plates implies a stress regime on arc systems. Stress is released usually through dislocation textures (e.g. kink bands, undulose extinctions and subgrain formation). Advanced releases in stress can often result in Crystallographic Preferred Orientation (CPO's). For example, Ionov, (2010, Avacha peridotites) found the pockets of finer grains to be the same minerals as those coarse grained, albiet with slightly less orthopyroxene present. Ionov suggested this texture change was produced by fracturing and

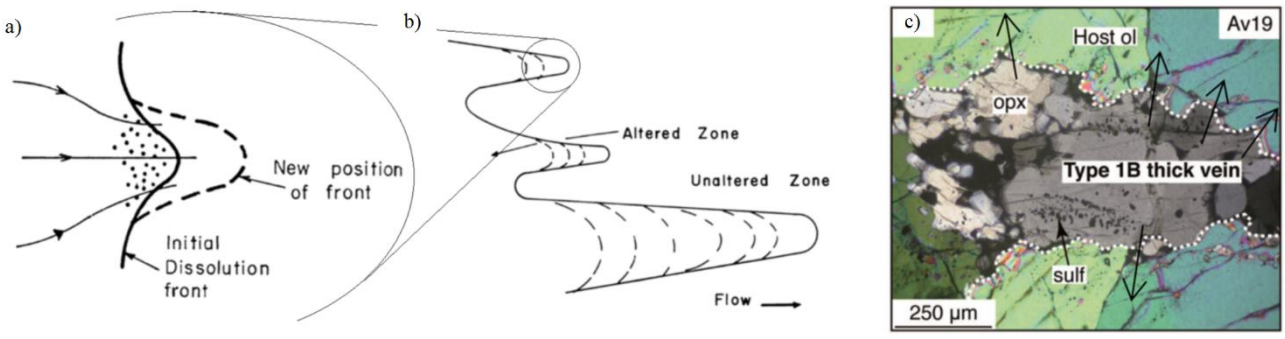

Figure 2.4: a-b) Schematic showing dissolution and moving boundary in reactive instabilities after Ortoleva et al. (1987). c) XPL photomicrograph as in Figure 3c, note black arrows showing direction of flow as prescribed in Figure 4a-b, after Bénard and Ionov (2013).

recystallisation of the host induced by the stress regime of the subduction system, rather than a metasomatic feature. Plausibly, the result of this process are pockets of finer grains and CPO in the mantle wedge (e.g. Imon et al., 2004; Bail and Trepmann, 2013; Arai and Ishimaru, 2008).

Interestingly, CPO's have shown to be the result of DPC and not necessarily the result of dislocation creep (e.g. Bond and den Brok, 2000). Exhumed arc systems (arc terranes) show that DPC deformation is not wide spread, but localized to the subducting slab- mantle contact (Figure 2.1) and in confined shear zones acting as fluid pathways (e.g. Gerya and Stöckhert, 2002). Evidently, a combination of petrographic and geochemical studies are required for a complete context behind xenolith history.

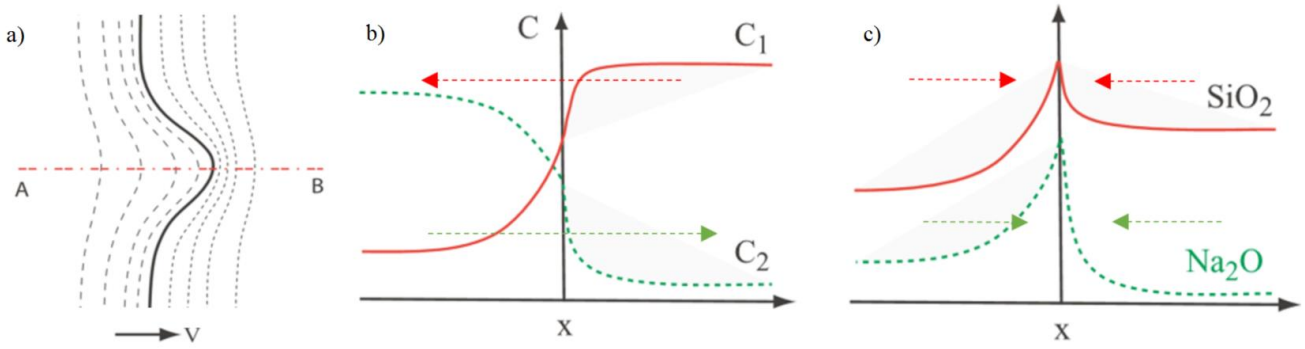

Figure 2.5: a schematic showing the effects of concentration profiles across a boundary adapted from Liang and Guo (2003). a) Diagram showing an imaginary profile across a boundary, with contours showing relative concentration of elemental abundance. b) Stabilization of the reaction would occur when material is transported across the boundary. c) Destabilization and further reaction would occur when material move into the boundary.

2.3. Batan Island, A Natural Laboratory

Batan Island is one of many volcanic islands located in the Batanes - the northern most point of the Philippines - lying between the main island of the Philippines and Taiwan. Stretching the length of sea between Taiwan and the main island of the Philippines is the Luzon arc (Figure 2.6a). The arc has a complex tectonic history: subduction of an extinct mid-ocean spreading ridge resulted in an eastward shift, and rotation of the volcanic arc (Figure 2.6a, refer to Yang et al., 1996). Batan Island is at the junction of the two volcanic chains.

Batan is built by two volcanoes, two of which build the islands topography: Mt Maratem to the south; and Mt Iraya to the north (Figure 2.6b). Lavas on Batan vary from basaltic to andesitic, with hornblende occasionally a phenocryst phase in erupted lavas (Sajona et al., 2000, Figure 2.6b). Interestingly, many of the lavas <2 ma have high K calc-alkaline andesitic signature (e.g. Defant et al., 1990), suggesting the magmatic

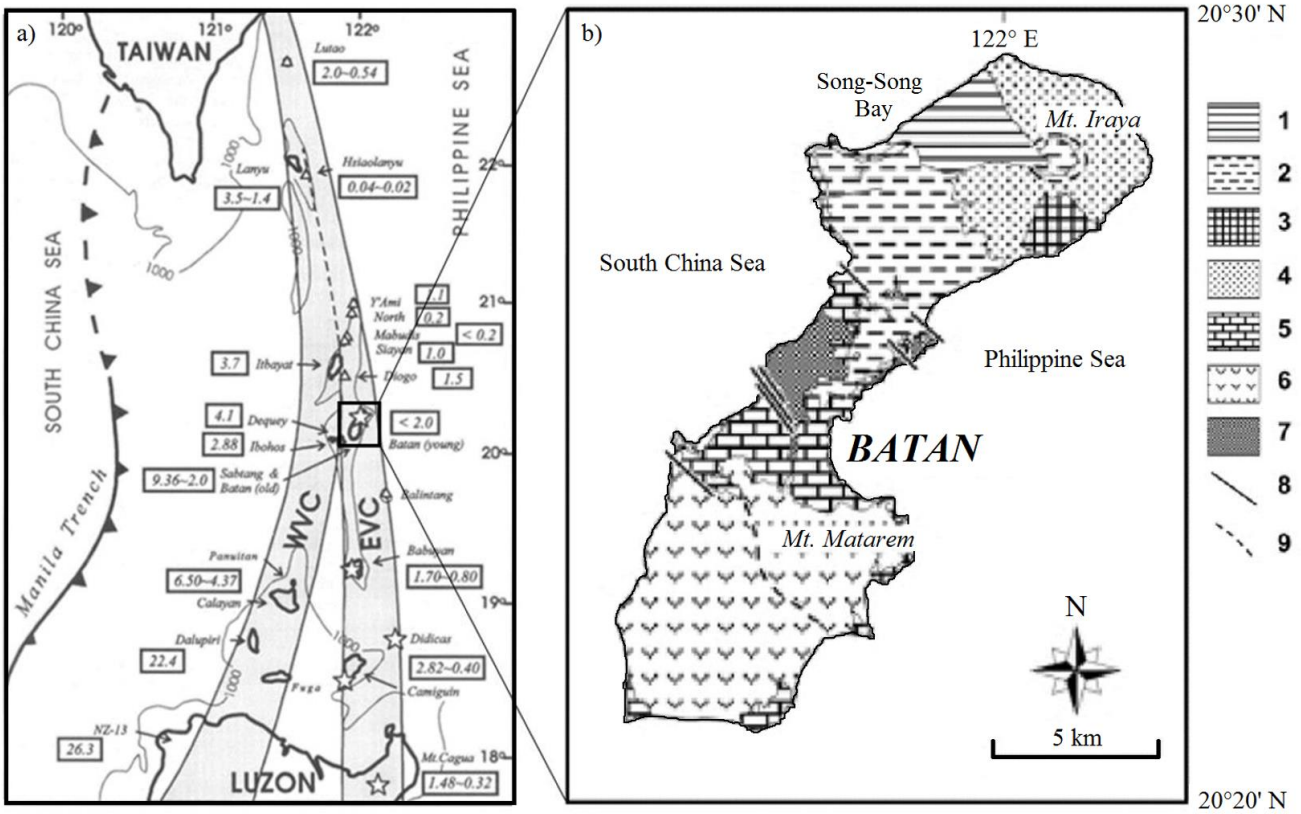

Figure 2.6: a) Tectonic map of Luzon arc showing the Western Volcanic Chain (WVC) and younger Eastern Volcanic Chain (EVC) with subduction orientations after Yang et al., 1996. b) Simplified geology of Batan Island after Sajona et al., 2000. KEY: 1. Youngest phase volcanics with mantle wedge xenoliths. 2. Pyroclastic flow deposits (2.5-1.7 Ka). 3. Hornblende andesite (1 Ma). 4. Basaltic to andesitic lavas with some pyroclastic flows. 5. Limestone. 6. Maratem volcanics (6.0-1.7 Ma). 7. Oldest volcanics. 8. Fault lines. 9. Caldera rim.

system beneath Batan is highly evolved and fractionated. Many of the lavas on Batan represent adakites or transitional adakites, suggesting a strong influence of slab-derived melts (e.g. Maury et al., 1992; McDermott et al., 1993; Schiano et al., 1995). Mt Iraya, is well known for its high frequency of mantle wedge xenoliths entrained in erupted lavas. The youngest phase of volcanics (McDermott et al., 1993) has a high frequency of composite mantle xenoliths entrained in the lava, which can be collected in cliffs along Song-Song Bay (Figure 2.6b).

The peridotite nodules have been heavily studied in literature (e.g. Maury et al., 1992; Schiano et al., 1995; Turner et al., 2012; Fourcade et al., 1994; Vidal et al., 1989; Arai et al., 1996; Arai and Kida, 2000; Arai et al., 2004). Defined as a harzburgite (e.g. Arai et al., 1996) the nodules have been strongly influenced by slab derived melts (e.g. Maury et al., 1992; Schiano et al., 1995; Fourcade et al., 1994; Turner et al., 2012). Trace element patterns have suggested a high H_2O content (e.g. Vidal et al., 1989) whilst isotope systems (e.g. Sr, Nd and Pb) suggest a high degree of sediment influence (e.g. McDermott et al., 1993; Turner et al.,

2012). Furthermore, there is a striking correlation in whole rock trace element data between these composite xenoliths and the host lavas (Figure 2.2a; Turner et al., 2012; Maury et al., 1992).

The mantle wedge under Batan Island also shows similar grainsize variations as those in Figure 2.3b and described by Ionov (2010) in Avacha peridotites. The grainsize variation was first noted by Arai et al. (1996), and appropriately characterized the nodules into F-Type (fine) and C-Type (course). Arai et al. (2004) proposed the change in grainsize was the result of shear zones acting as fluid pathways. Plausibly, this is the same DPC deformation process as described by Gerya and Stöckhert (2002). Although variable in grainsize, each harzburgite nodule is encompassed by coarse grained, amphibole (e.g. Arai and Kida, 2000; Arai et al., 2004).

3. Aims of Study

The occurrence of amphibole in these composite xenoliths has only been mentioned in selected literature (e.g. Arai and Kida, 2000; Arai et al., 2004). Therefore, the full context surrounding the harzburgite nodules has not been fully addressed. Given this gap in knowledge, this body of work combines petrographic and geochemical techniques to answer the following questions:

- How did the xenolith form?
- At what Pressure-Temperature (P-T) conditions did the amphibolite and amphibole gabbro form?
- What relationship is there between the three components in P-T space, physically and chemically?
- What is the relationship (if any) between these composite xenoliths and their host lava?

Interestingly, the host lava contains no amphibole, yet the composite xenoliths contain amphiboles in all three components. There is also a large discrepancy between the occurrence of amphibole in arc terranes and not in the majority of arc lavas. This is puzzling. Trace element data from erupted arc lavas has been used to argue for the importance of amphibole in arc lava petrogenesis (e.g. Davidson et al., 2007 and 2013). Appropriately, the importance of amphibole was termed cryptic (e.g. Davidson et al., 2007; Smith, 2014) as no physical evidence showed a relationship between amphibole, melt and host rock. Some literature has suggested amphibole is a reaction feature within the magma chamber (e.g. Krügel, 1998). However, since amphibole does not occur as a phenocryst phase in the host lava that may not be the case.

Since the xenoliths from Batan Island show such interesting features and a possible relationship between amphibole and the peridotite nodules, this body of work also aims to provide a physical conclusion to the importance of amphibole in arc lava petrogenesis as suggested by Davidson et al. (2007 and 2013).

4. Methods

4.1. Petrographic analysis

Preliminary electron backscatter (BS) imaging and Energy Dispersive X-Ray Spectrometry (EDS) chemical mapping of two thin sections (xenolith and host lava, Appendix 1, Figure 1 and 2 respectively) was conducted on the Hitachi TM3030 Scanning Electron Microscope (SEM) at the Australian National Fabrication Facility (ANFF), Australian Hearing Hub, Macquarie University. Instrument conditions were consistent across the two analysis sessions. Each map was constructed after 60 seconds of analysis with an accelerating voltage of 15 keV. The elements targeted in both samples were O, C, Si, Mg, Fe, Al, Ca, Na, Ti and K.

Secondary, higher resolution analyses of the xenolith thin section was conducted on the Zeiss EVO MA15 SEM, GEMOC, Geochemical Analytical Unit (GAU) at Macquarie University. This SEM has Cathodoluminescense (CL) imaging, EDS and Electron Backscatter Diffraction (EBSD) capabilities. EBSD and EDS analyses ran simultaneously. Operating conditions remained the same over multiple analysis sessions with an accelerating voltage of 15 keV and 3 nA beam current. Working distance ranged from 10 mm to 22.5 mm and the sample was placed on a 70° gradient. The length of analysis was dependent on the step size and area of the map. Initial analysis was at a step size of 20 µm for large scale, fast analysis to understand what needed to be targeted for higher resolution analysis. Maps constructed during the second analysis were at 4 µm step sizes, except for CPO of hornblende and anorthite only which had a 10 µm step size resolution. The elements targeted in the EDS analysis were O, C, Si, Mg, Fe, Al, Ca, Na, Ti, Cr and K. Post processing was conducted on Channel5 Mambo and Tango software packages were used to resolve data.

4.2. Elemental analysis

In situ analysis of two thin sections (xenolith and host lava) for major element abundances of hornblende, plagioclase, clinopyroxene, orthopyroxene and olivine were measured by Wavelength Dispersive Spectrometry (WDS) using a Cameca SX 100 Electron Microprobe (EMP) at GEMOC, GAU, Macquarie University. On both occasions, each analysis ran for 5 min 6 sec and the operating conditions did not vary with a 15 keV accelerating voltage, 20 nA beam current and a beam size of 1-2 µm. The EMP was calibrated through analysis of natural and synthetic materials. Each analysis point of the sample were selected based on

petrographic analysis and BSE detector imagery. Visible defects in the mineral, holes and cracks were avoided. Chemical formulae was calculated from weight percent oxide data (refer to Deer et al., 1992) to check legitimacy of totals from the analysis.

In situ analysis of the xenolith 60 μm thick thin section for trace element abundances was conducted using Laser-Ablation Inductively-Coupled-Plasma Mass-Spectrometry (LA-ICP-MS) at GEMOC, GAU, Macquarie University. Analysis was conducted using a Photon Machines Excite 193 nm Eximer laser coupled to an Agilent Technologies 7700 Series quadropole ICP-MS. Excimer laser ablation operated at 15 kV over a 50 μm spot size with a Burst Rep Rate of 5 Hz at a fluence of 7.59 j/cm^2. A spot size of 40 μm was used where a 50 μm spot size was too large. The ablated sample transported by an argon carrier gas, was ionized through an ion plasma, analyzed through the quadrupole mass spectrometer for 30 seconds time off, 60 sec on background and 120 seconds on sample.

NIST610 glass was used as a calibration standard, and several materials (BHVO-2G and BCR-2G glasses and NIST610) were used as reference materials to check accuracy and precision. Averaged SiO2 wt. % data collected on the EMP was used to calibrate unknown points. "Glitter!" software package was used to correct for instrumental drift and signal filtering.

4.3. Dingo- Neutron Tomography

This novel technique provides 3-dimensional reconstructions, showing physical relationships on the hand sample scale without further destruction to the sample. The technique - developed at the Australian Nuclear Science and Technology Organization (ANSTO, Lucas Heights, Sydney) - fires neutrons at a sample. Density contrasts are directly proportional to the neutron intensity allowed to pass through the sample. Therefore, an image of the neutron 'shadow' can be taken. The sample (Appendix 1, Figure 3) was placed on a stage which rotates, pausing every 0.02 degrees for sequential neutron shadow images to be taken. A total of 1859 images were taken. These were rendered in "AVISO" and "VG Studio" for 3-dimensional constructions.

5. Results

5.1. General sample description and Neutron Tomography

The development of neutron tomography (NT, Dingo) at ANSTO has made it possible to analyze the inner morphology of the sample without any further destruction. This is especially important in this study due to the precious nature of the sample. An important feature of the neutron tomography reconstructions is the added ability to view the sample in 3 dimensions, and to slice the reconstructed image similar to a C-T scan.

Each components morphology differs. 3-dimensional reconstructions reveal interesting features shown in Figure 5.1. Grey scale variations (Figure 5.1b) clearly depict the three components (i.e. peridotite nodules, hornblendite rind and hornblende gabbro) which has been linked to the photograph in Figure 5.1a. Several features need to be highlighted. The peridotite components are fragments, suggested on hand sample (Figure 5.1a) and clearly depicted by slicing a 3D reconstruction in Figure 5.1b and c). Peridotite fragments are always encompassed by a hornblendite rind (between red and yellow dashed lines). Furthermore, the thickness of hornblendite armors on fragments varies.

Consequently, the hornblende gabbro is never in contact with the peridotite fragments and the irregularity of fragment orientation has influenced the amoeboid shape of the hornblende gabbro.

5.2. Petrography and quantitative spatial analysis

5.2.1. Peridotite fragments.

The peridotite fragments have interesting microstructures. Fragments have an unusual mineral assemblage: olivine (78%), clinopyroxene (8%), hornblende (7%), orthopyroxene (6%), spinel (~1%) and glass (<1%). Coarse grained olivine microstructures show crystal plastic deformation as undulose extinctions, kink bands and subgrain formation (Figure 5.2a and c). Among the deformed olivine are pockets of much finer grainsizes and single grained "veinlets" (Figure 5.2c-d). The term 'veinlet' is used here as the vein is not a typical fracture-fill propogation of a vein, rather the fluid is confined to pre-existing defects in olivine.

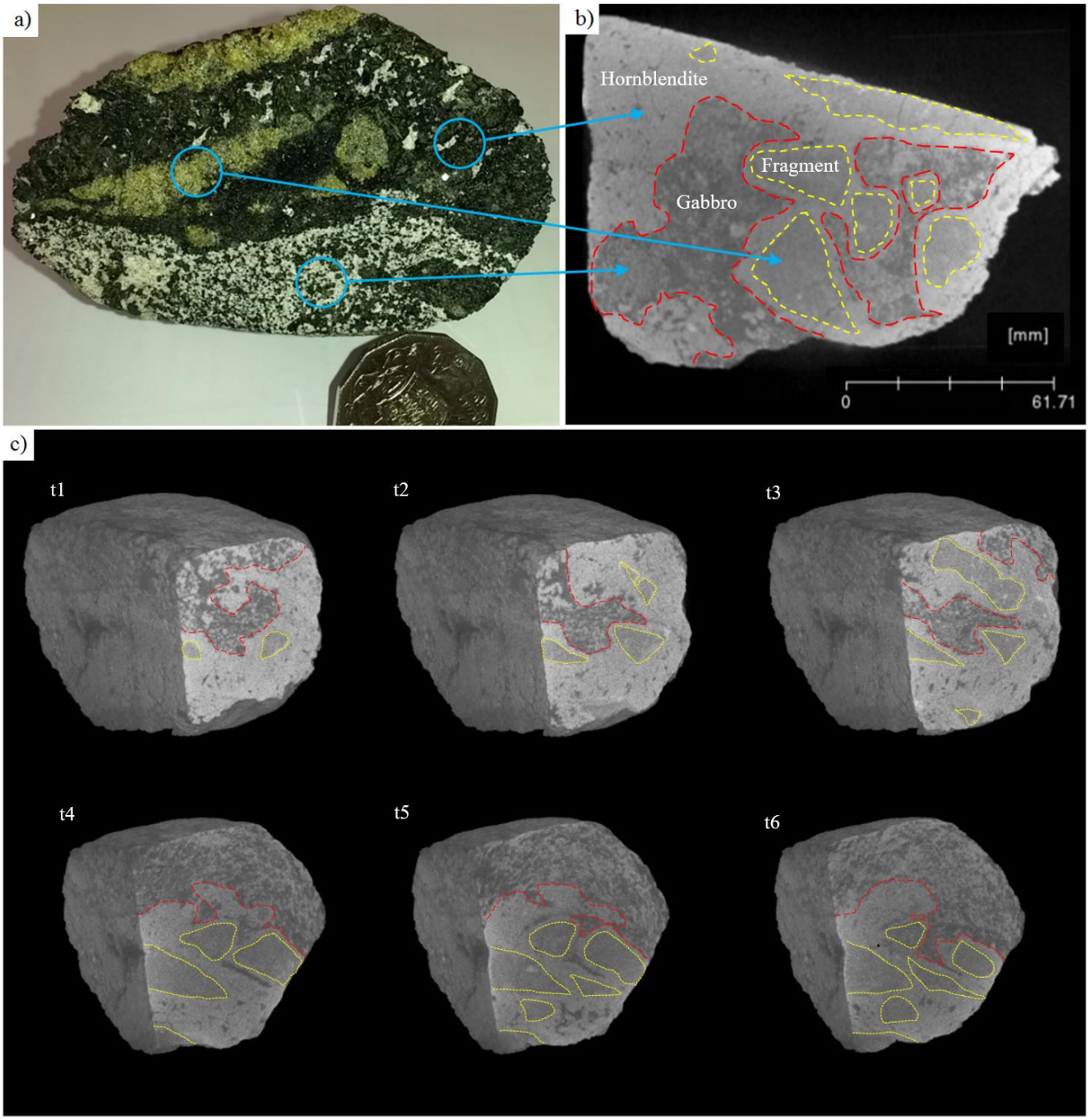

Figure 5.1: The power of rock C-T scanning. a) Photograph of the hand sample imaged in DINGO with an AUD 50c piece for scale. Blue arrows point to corresponding components in (b). Darkest colours are plagioclase, lightest are hornblende. Peridotite fragments are the middle ground. Red dashed line denotes the boundary between gabbro and hornblendite. Yellow dashed line denotes boundary between peridotite and hornblendite. c) A representative sequence of xenolith slices, where 't' is an arbitrary measure of slicing along the xenolith reconstruction.

Importantly, the fine grained pockets (5.2a) have a much higher modal proportion of hornblende, clinopyroxene and spinel. Furthermore, spinel has the smallest grainsize and is often associated with the

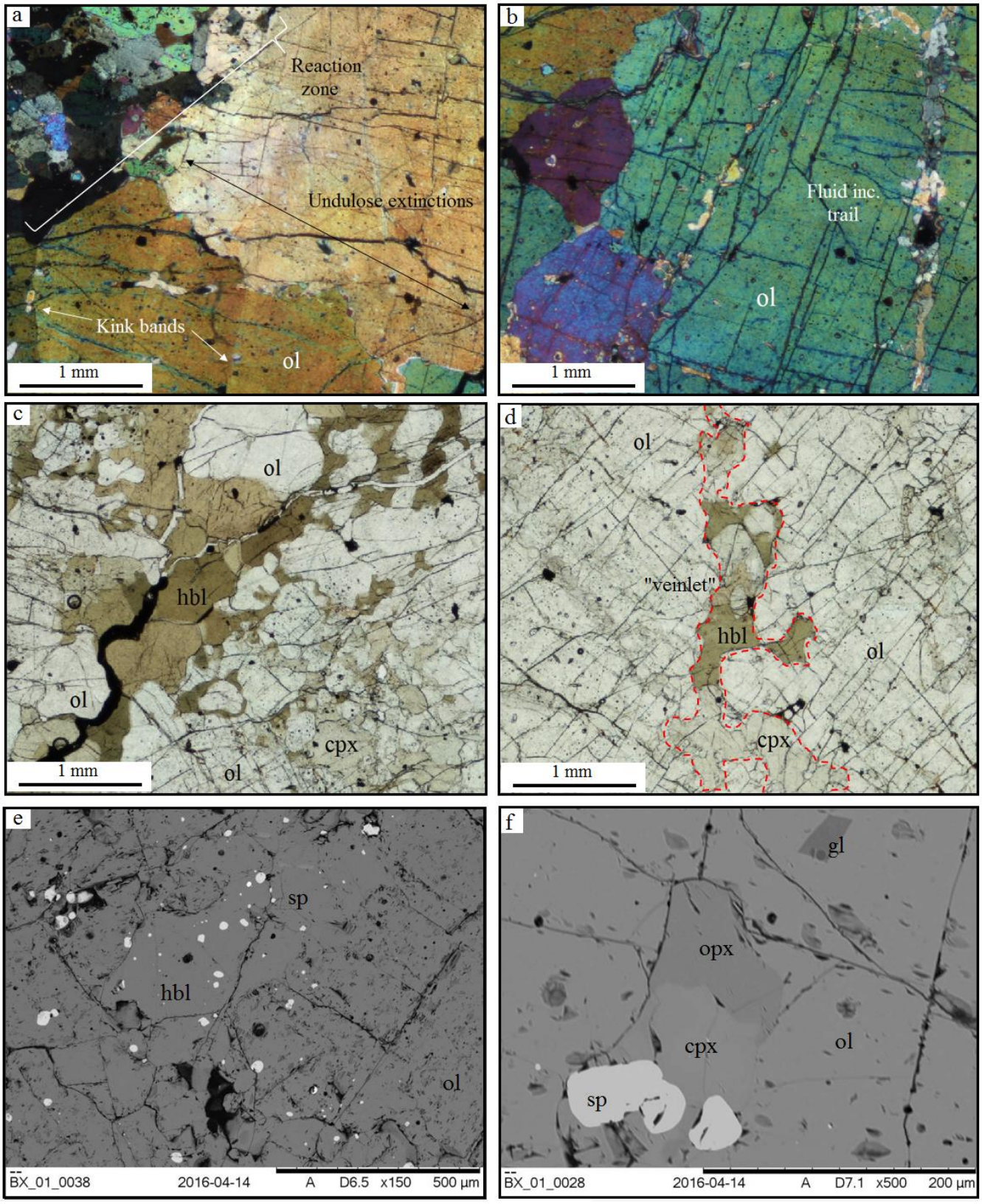

Figure 5.2: petrographic relationships within the peridotite fragments. a) XPL image showing crystal lattice defects in undulose extinction and kind bands within olivine (ol) as well as a fine grain pocket (reaction zone) with hornblende (hbl) clinopyroxene (cpx) and some spinel (sp). b) XPL image showing a fluid inclusion trail (mostly orthopyroxene) to the right and olivine subgrains to the left. c-d) PPL images of single grain hornblende-clinopyroxene veinlets. c) Note how hornblende encapsulates olivine

subgrains. d) Shows the form of an incipient 'veinlet' infiltrating through olivine. e-f) BSE images at higher resolution than photomicrographs. e) Fine grained spinel are inclusions in hornblende. Olivine is easily identified by the 'dirty' texture as a result of crystal lattice dislocations. f) In olivine, spinel is usually associated with clinopyroxene and orthopyroxene. Glass (gl) inclusions are also present (as described in Schiano et al., 1995). Glass inclusions are also found at the junction between olivine and orthopyroxene.

lattice defect free hornblende (5.2e). Importantly, clinopyroxene also exhibits a lack of crystal plastic deformation. Thus, hornblende and clinopyroxene must have crystallized after crystal lattice deformation had occurred in the olivine and a secondary feature to the fragments.

The single grained veinlets (Figure 5.2c-d) are not typical fluid filled fractures. Both clinopyroxene and hornblende create sublinear features across fragments infiltrating along defects in the olivine (Figure 5.2c) and around subgrains (Figure 5.2d). Like in the fine grained pockets, clinopyroxene and hornblende exhibit a lack of crystal plastic deformation. Interestingly, adjacent olivine tends to share the same lack of dislocation features (Figure 5.2c).

5.2.2. Hornblendite rind and melt-rock reaction.

The hornblende rind is an interesting feature of these xenoliths and importantly, the rind varies on microstructure scale. The neutron tomography 3 dimensional reconstructions explicitly show that every fragment is encompassed by hornblende (5.1b and c). Figure 5.1b not only shows thin hornblendite separating the fragments from the gabbro (top right), but there is also a large section of hornblendite surrounding a very small fragment (bottom left).

In a single thin section, hornblendite microstructures vary dramatically (Figure 5.3). These microstructures show the hornblendite crystallized rapidly and aggressively. Firstly consider the grainsize difference in the hornblende between Figures 5.3a and e. The coarse grained hornblendite has decussate textures and euhedral growth (b). Decussate textures are an energy efficient method of crystal growth. Conversely, the embayed nature of the peridotite-hornblendite contact (c) and high frequency of inclusions and lack of crystal form (d) suggests a very fast rate of crystallization. Furthermore, the relict olivine (d) suggests the reaction is engulfing the fragments as well.

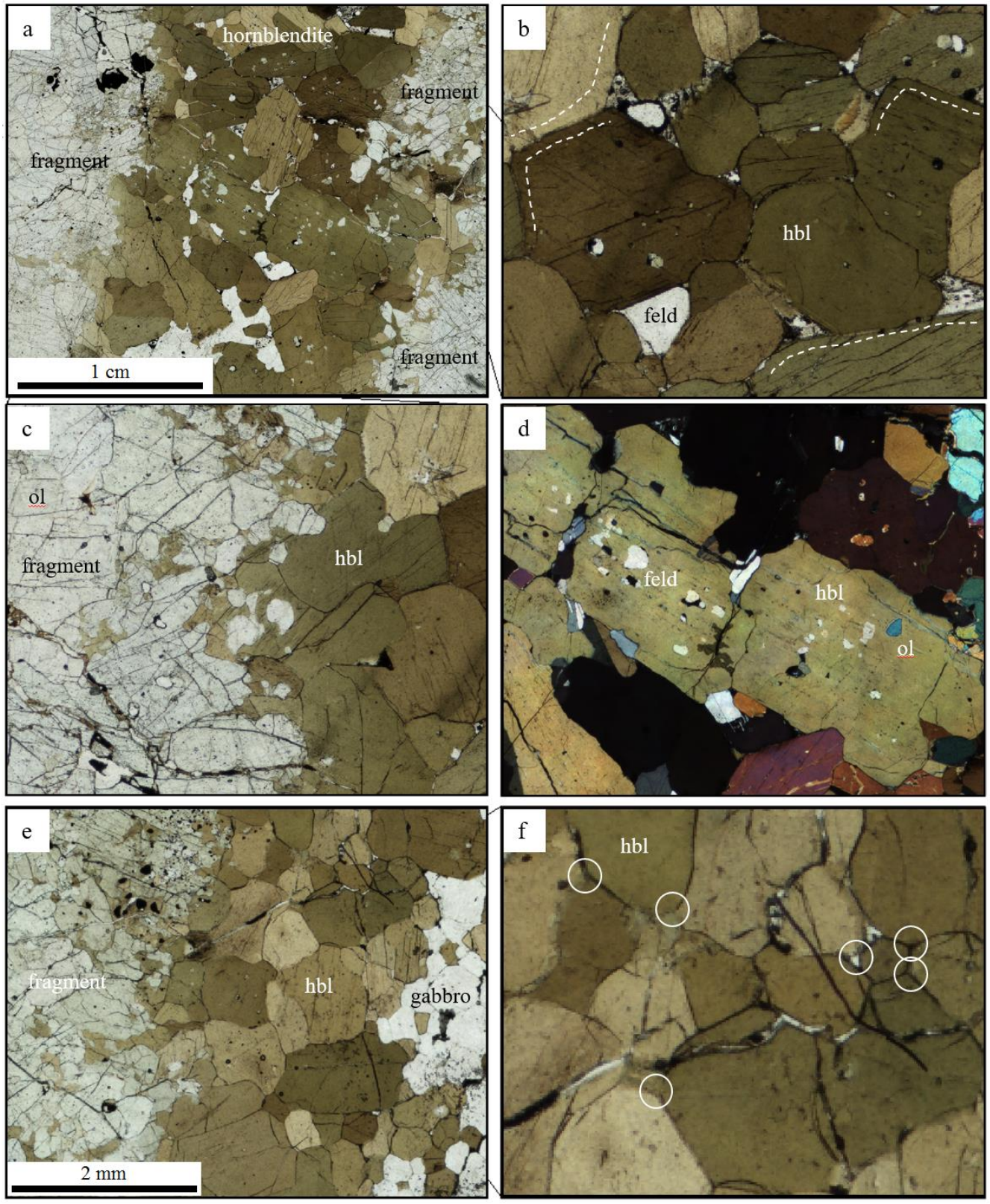

FIGURE 5.3: Photomicrographs of hornblendite features. a) PPL image of coarse grained hornblendite. 'Fragment" refers to peridotite component. b) PPL image showing euhedral, decussate features (white dashed line) in hornblende (hbl), and plagioclase (feld) inclusions. c) PPL image showing embayed nature of hornblendite-fragment contact. d) XPL image showing sub-euhedral, very large hornblende with plagioclase (feld) and olivine (ol) inclusions. e) PPL image of fine grained hornblendite separating gabbro and fragment. f) PPL image zoomed in on fine grained hornblendite showing 120 triple junctions and no inclusions.

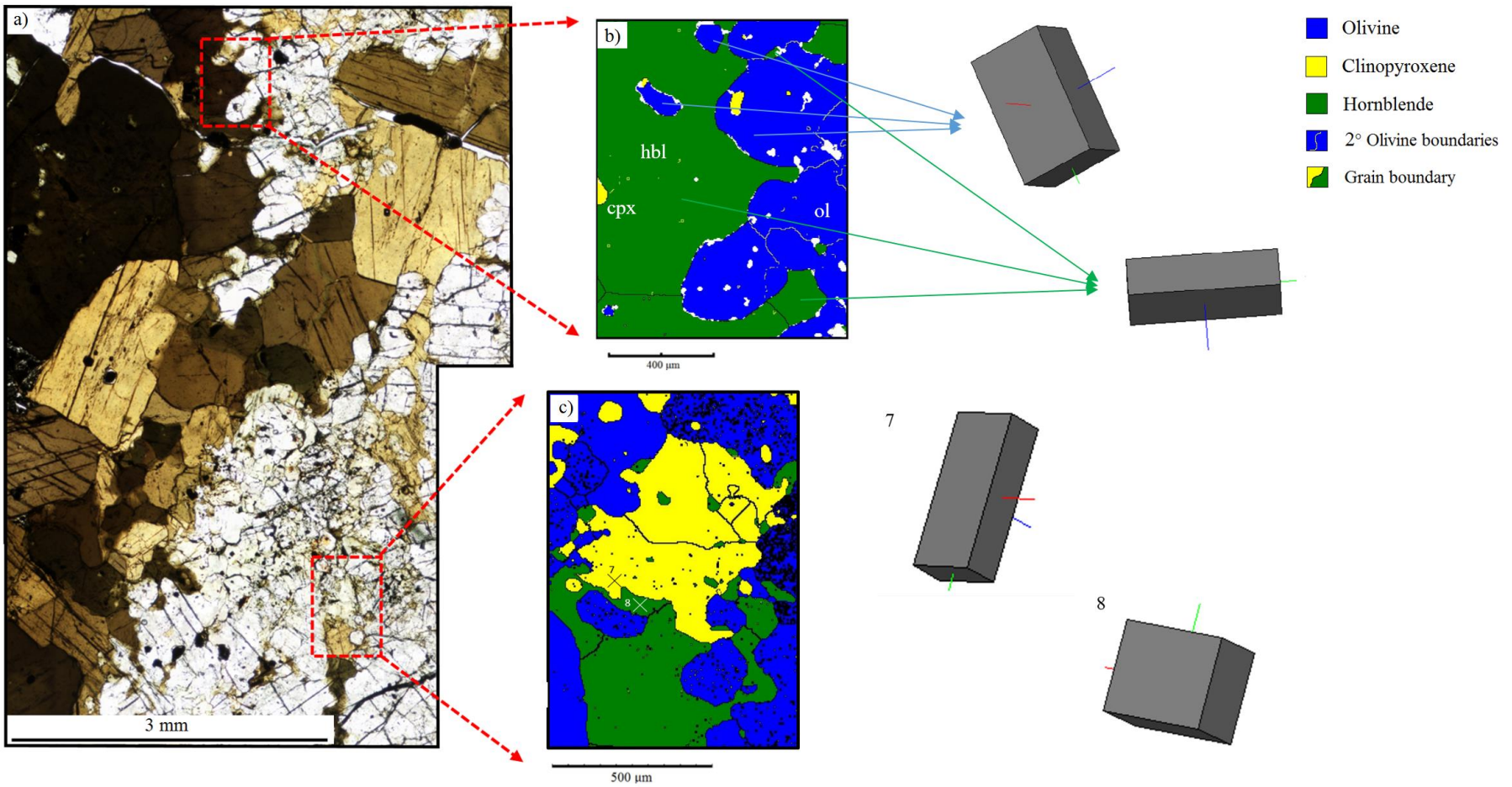

Figure 5.4: EBSD images showing infiltration relationships between hornblende, clinopyroxene and olivine. a) PPL image showing location of EBSD maps in (b) and (c). b) Mineral phase map at the peridotite fragment-hornblendite contact. Three locations for olivine (ol) and hornblende (hbl) point to a particular 3-d prism illustrating crystal orientation. In this case, all three for both minerals have the same orientation. b) Mineral phase map along a single grain veinlet. Clinopyroxene (cpx) and hornblende have very similar crystal orientations.

Contrast the high frequency of inclusions in (d) and decussate textures in (b) with the total lack of these features in the finer-grained hornblendite separating fragments with gabbro (e). Importantly, the identification of 120° triple junction (red ellipses, Figure 5.3f) are typical annealing microstructures, suggesting this part of the rind was kept hot for longer.

It is crucial to realize that whilst the microstructures are different, the contact relationship between peridotite fragment and hornblendite remain the same across Figure 5.3a and e. This similarity suggest that factors external to the melt-peridotite relationship are the result of the grainsize variation.

EBSD has been used to define the physical relationship between hornblende and peridotite fragments. Figure 5.3c and e clearly show the embayed contact on a thin section scale. However, the higher resolution EBSD results in Figure 5.4 show the relationship in greater detail. Crucially, the relationship between hornblende and olivine is the same regardless of position (i.e. at the hornblendite-peridotite contact or as a single grain veinlet (Figure 5.4b and c respectively). Clearly, both insets show the melt exploiting crystal defects in olivine. Importantly, two subgrains and the main body of olivine have identical crustal orientations. Furthermore, three hornblende grains also sharre the same crystallographic orientation demonstrating how these hornblende grains could be one grain in 3 dimensions. Interestingly, adjacent clinopyroxene and hornblende (Figure 5.4c) also have the same crystallographic orientation. This demonstrates simultaneous growth.

5.2.3. Hornblende Gabbro

The hornblende gabbro has a much finer grainsize, is never in contact with the peridotite fragments and the amoeboid structure looks to be influenced by the sporadic spatial nature of the peridotite fragments (Figure 5.1). Microstructures (Figure 5.5) are also completely different to the peridotite fragments and hornblende rind.

A crystallographic preferred orientation is defined in both 100 and 010 axis for Hbl and anorthite (Figure 5.5c). Furthermore, the same 120° triple junctions in the smaller hornblendite (Figure 5.3f) are more prevalent in the gabbro (red ellipses in Figure 5.5b).

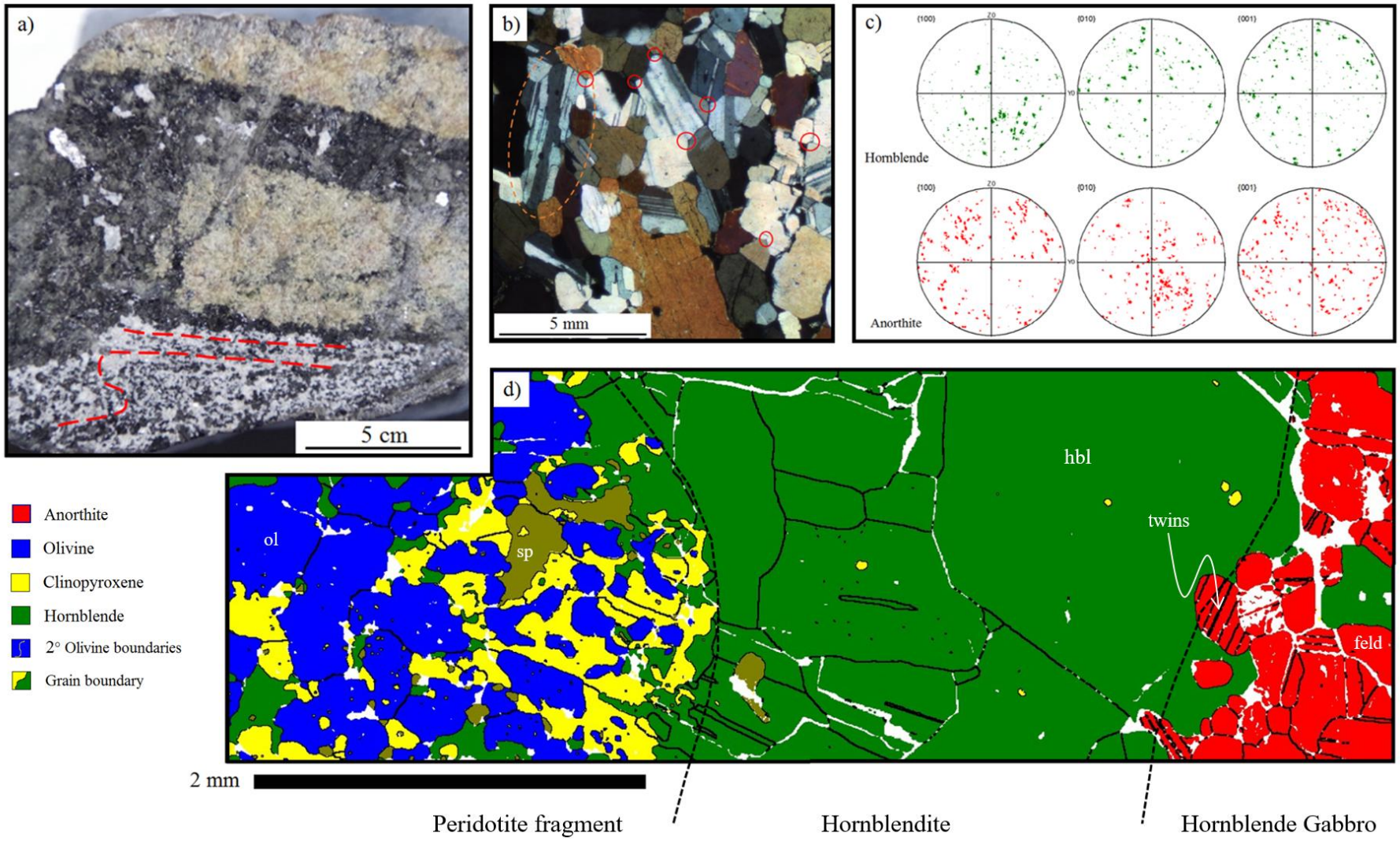

Figure 5.5: a) Photograph of the hand sample, red dashed lines are to show a preferred orientation within the gabbro. b) XPL image of the gabbro highlighting 120° triple junctions (red ellipses) and elongate plagioclase (orange dashed ellipse). c) Pole figures for a-axis (100), b-axis (010) and c-axis (001) for hornblende (green) and anorthite (red). d) EBSD mineral phase map crossing both contacts.

The contact between the gabbro and hornblendite rind demonstrates a different relationship to the peridotite – hornblendite rind contact. Anorthite and hornblende do not exploit grain boundaries and defects in this contact as hornblende and clinopyroxene does at the fragment – hornblendite rind contact. Instead, the contact is defined by interlocking textures (Figure 5.4d).

5.3. Composite Xenolith- Mineral Chemistry

5.3.1. Major element concentrations

Major element concentrations and calculated structural formula for representative mineral phases in the composite xenolith are presented in Appendix 2, Tables 1-5.

Structural formulae of hornblendes categorise them as pargasitic compositions (Leake et al., 1997; Appendix 2, Table 1). Hornblendes are very calcic (11.63-12.46 wt. % ox.) with TiO_2, $Mg_{\#}$, K and Na (apfu) concentrations varying relative to which component of the xenolith the hornblende grain lies (Figure 5.6a and b). As such, TiO_2 content decreases when the $Mg_{\#}$ of hornblende increases in a linear fashion (Figure 5.6a). Similar trends are seen with variation in relative proportions of K and Na against TiO_2 (Figure 5.6b). Partitioning of K and Na has stemmed from a point (red). Importantly, the hornblendes within the gabbro (red) are completely separate to those within the peridotite fragments (black). Variation related to position in the composite xenolith is also seen in Cr. Although, commonly below detection limits in hornblendes from the gabbro and hornblendite, Cr is found in hornblendes within peridotite fragments (e.g. 0.822 wt. % ox., Table 5.1), especially those with engulfing spinel within reaction zones. Importantly, hornblendes major element variation in the peridotite can be traced to a particular point (composition of hornblende in the gabbro).

Representative analyses of olivine is presented in Appendix 2, Table 2. Olivine is Fe rich forsterite with $Fo_{\#}$ ranging from $Fo_{78.4\text{-}81.7}$. Interestingly, there are two populations of $Fo_{\#}$s (Figure 5.6c). Slightly higher $Fo_{\#}$ numbers were found in olivines from the second peridotite fragment in thin section (Appendix 1 Figure 1). Both MnO and NiO show considerable variation (0.40-0.44 and 0.19-0.30 wt. % ox. Respectively). However, neither show any correlation with $Mg_{\#}$. The melt inclusions in olivine (Figure 5.2f) are adakitic (Schiano et al., 1995) and major element chemistry is presented in Appendix 2, Table 6. Si and Al rich (~64 and ~19 wt. % ox. respectively), the melt inclusions are alkali rich with NaO_2 (5.31-5.65 %), CaO_2 (4.01-4.24 %) and, K_2O (3.91-3.96 %), importantly, in high abundance.

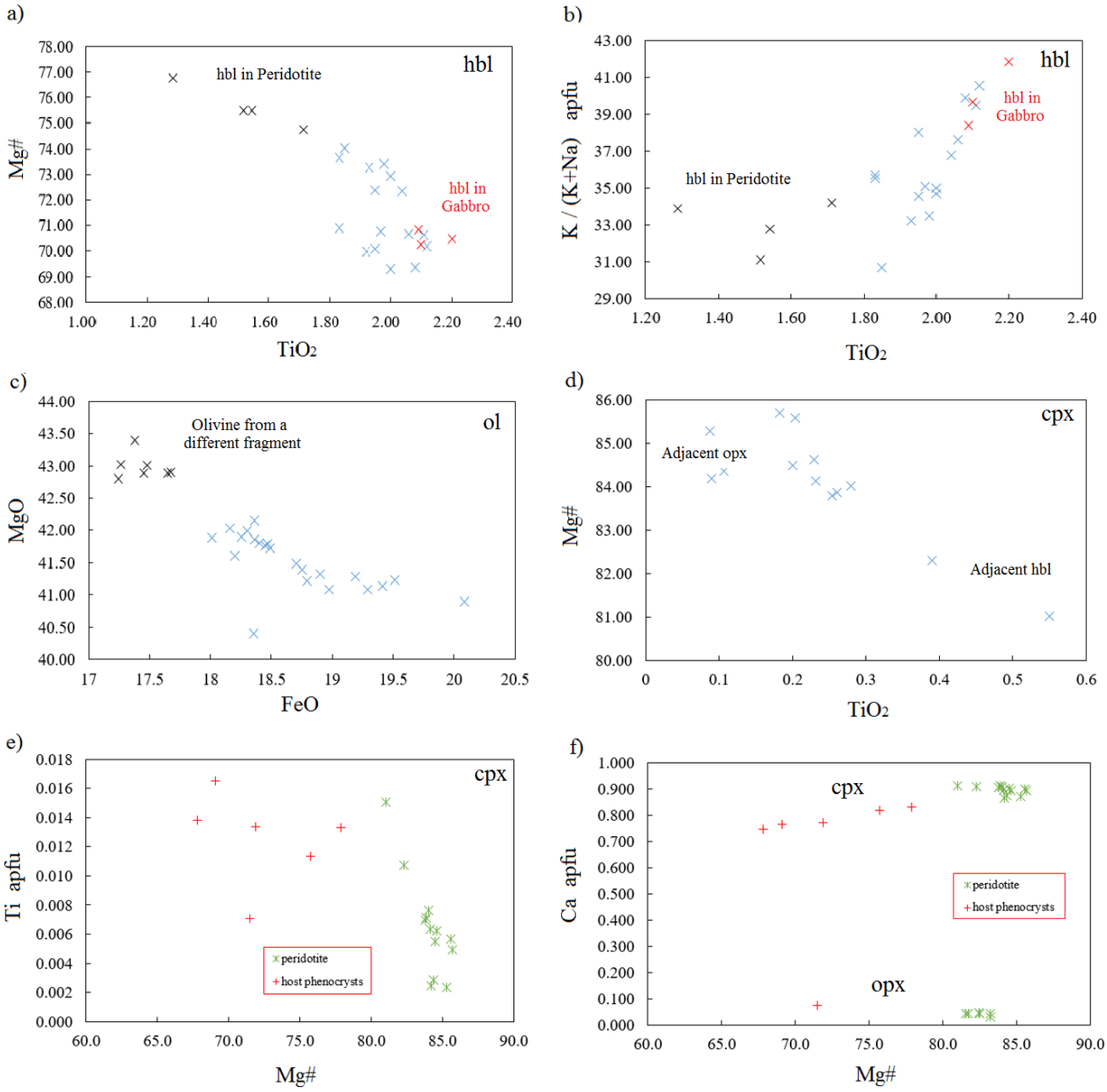

Figure 5.6: Major element plots showing significant spatial trends. a) Mg# (Mg# = atomic number Mg*100/ (Mg + Fe (t)) vs TiO_2 content for hornblende (hbl) within the xenolith. Black points are hornblende grains within peridotite fragments, red points are hornblendes within the gabbro component. b) Relative proportions of K to Na vs TiO_2 content in hornblende from the xenolith. "apfu" is atoms per unit formula. Coloured points as in (a). c) MgO vs FeO for olivine from the xenolith. d) Mg# against TiO_2 for clinopyroxene (cpx) from the xenolith. e) Ti (apfu) against Mg# for clinopyroxene from both xenolith and host andesite. f) Ca (apfu) against Mg# for clinopyroxene and orthopyroxene (opx) in both xenolith and host andesite.

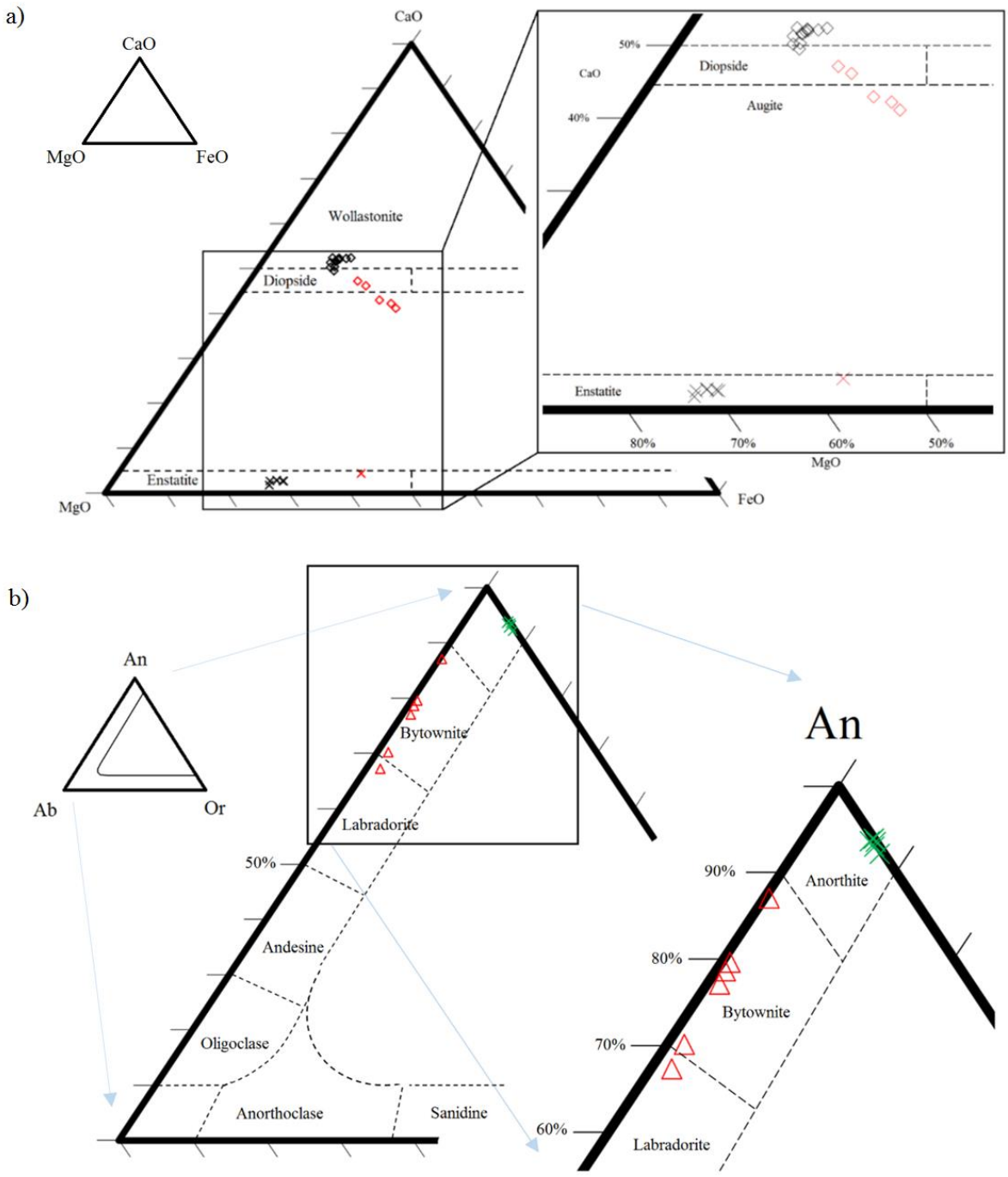

Figure 5.7: a) End-member ternary for pyroxene. Diamonds are clinopyroxene, crosses are orthopyroxene. Black points refer to pyroxenes from the xenolith, red from the host lava. b): Plagioclase An-Ab-Or ternary plot. Plagioclase from the xenolith are plotted as green crossed, from the host andesite as red triangles.

Representative analyses for both clinopyroxene and orthopyroxene from the peridotite fragments is presented in Appendix 2 Table 3. Clinopyroxene is very calcic (diopsidic, Morimoto et al., 1989) and seldom varies (Figure 5.7a). However, $Mg_{\#}$ and TiO_2 contents do. The $Mg_{\#}$ of clinopyroxene shows an interesting trend relative to TiO_2 (Figure 5.6d). Higher concentrations of TiO_2 (0.39-0.55 %) were found in

clinopyroxene grains within single grained veinlets in the peridotite fragments, whilst those with lowest TiO_2 (~0.1%) had higher $Mg_{\#}$'s and were adjacent to orthopyroxene and spinel.

Orthopyroxene is enstatitic (Figure 5.7a) and does not show the same variations relative to its' neighbour as clinopyroxene does (e.g. Orthopyroxene adjacent to clinopyroxene or glass within olivine). Respectable concentrations of Al_2O_3 (0.55-1.11 %) and MnO (0.36-0.40 %) show no relative trend, either spatially or chemically.

Representative analyses of plagioclase is presented in Appendix 2 Table 5. Plagioclase is a mineral phase is found only sporadically in the hornblendite and within the hornblende gabbro. Structural formulae and relative Ca-Na-K contents categories plagioclase from both components of the xenolith as anorthite. Importantly, plagioclase is never in contact with the peridotite. Highly calcic, plagioclase $An_{\#}$ range between $An_{92.1\text{-}93.8}$ (Figure 5.7b). No noteworthy variation in major element abundances is seen between plagioclase from the gabbro or hornblendite.

5.3.2. Trace element abundances

Representative trace element abundances for the major mineral phases are shown in Appendix 3, Table 1. REE abundances for the five mineral phases (Figure 5.8a), deviate from a primitive mantle signature (e.g. McDonough and Sun, 1995).

Trace element signatures of the main mineral phases are shown in Figure 5.8a. Whilst olivine shows the greatest variation in trace element signature, olivine without any association with secondary minerals (e.g. hornblende and clinopyroxene) is enriched in LREE's and depleted in HREE's. Suspiciously, the extended trace element signature of olivine is mirrors whole rock trace element data of the host andesite (Figure 5.8d). Conversely, orthopyroxene are depleted in LREE's and enriched in HREE's. Metasomatic minerals show a very different trace element signature to olivine and orthopyroxene. A standout difference is the REE pattern of plagioclase. Positive anomalies in Sr and Eu are common with higher partition coefficients into plagioclase.

If experimental partition coefficients (e.g Adam and Green, 2006), of trace elements into minerals is representative of what occurs naturally, then the inverse of the partition coefficient can be applied to measured trace element abundances to calculate the equilibrium melt composition. With this assumption,

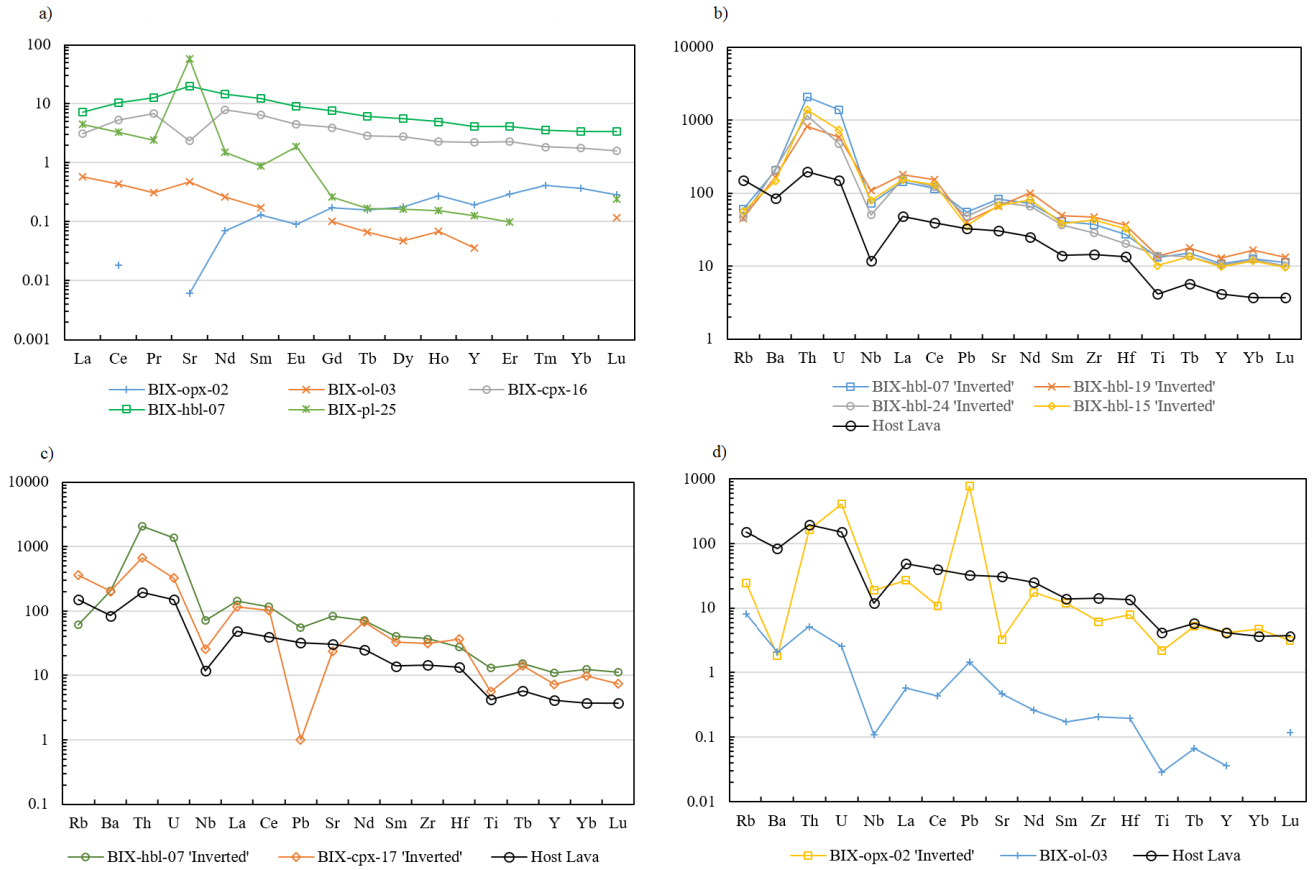

Figure 5.8: Primitive mantle normalized (McDonough and Sun, 1995) of single point analyses. a) REE + Y plot for the 5 major silicate mineral phases in the xenolith. b) Equilibrium melt composition plotted against whole rock trace element signature of the host andesite (from Turner et al., 2012). c) Equilibrium melt composition of clinopyroxene and hornblende against the host andesite. d) trace element signature of olivine and host andesite against the equilibrium melt composition of orthopyroxene. To calculate equilibrium melt composition, see text. Sample names (e.g. BIX-ol-03) refers to sample (BIX- Batan Island Xenolith), mineral (ol- Olivine, hbl- hornblende, pl-plagioclase, opx-orthopyroxene, cpx- clinopyroxene), 'Inverted' implies the equilibrium melt of that particular analysis.

the following equation has been applied to calculate the equilibrium melt compositions shown in Figure 5.8b-d. Importantly, partition coefficients vary between minerals, as such, care needs to be taken to apply the inverse partition coefficient of the same mineral.

$$\text{Initial composition}_X = X_{\text{mineral}} \times \frac{1}{K_d}$$

Where $X_{mineral}$ in ppm multiplied by the inverse of the partition coefficient (K_d) as defined by Adam and Green (2006) for that particular mineral will give the *Initial composition*$_X$ in ppm. These values have been normalized to Primitive Mantle (McDonough and Sun, 1995). This is a powerful tool because it implies that calculation of the melt responsible to the hornblendite rind and hornblende gabbro formation is possible.

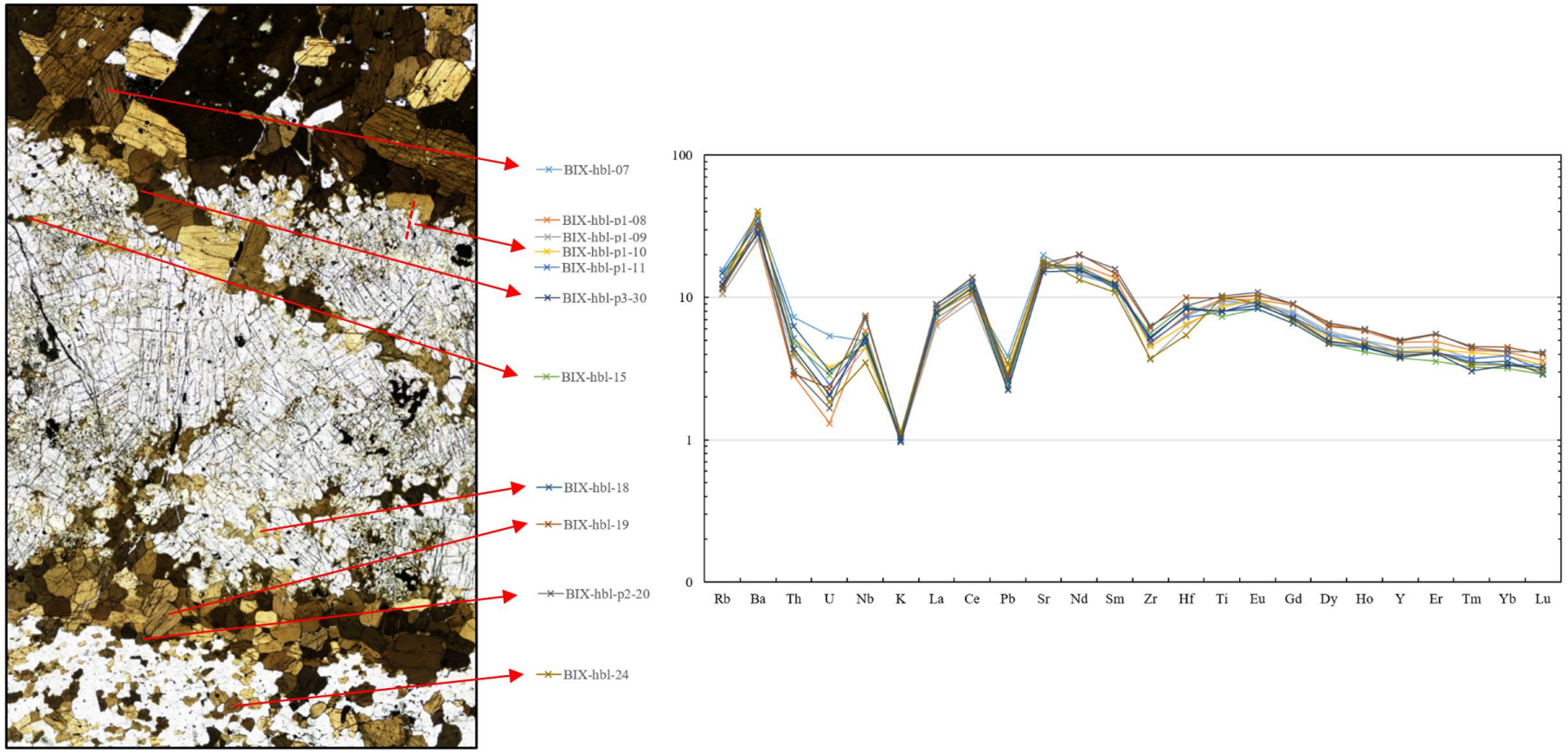

Figure 5.9: Locations of laser ablation pits linked to the extended trace element plot. Normalized to PM (McDonough and Sun, 1995). Analysis names are as in Figure 5.8.

Intriguingly, equilibrium melt compositions of hornblende from all xenolith components have the same signature (Figure 5.8a). Furthermore, aside from negative Rb and Pb anomalies, the signature mirrors the whole rock trace element signature of the host andesite. Interestingly, the equilibrium melt composition of clinopyroxene mirrors the hornblende equilibrium melt signature (Figure 5.8c), as does orthopyroxene (Figure 5.8d). The Pb anomalies in clinopyroxene and orthopyroxene are completely inverted relative to each other. When the same method was applied to olivine, there was no correlation.

Trace element signatures of hornblende does not show significant variation relative to which component of the xenolith the hornblende grain is, which is unlike the major element concentrations. Figure 5.9 shows the lack of variation clearly. Consistently, negative anomalies are seen in Rb, Th, U, K, Pb and Zr with positive anomalies in Ba and Nb.

5.4. Host Lava

5.4.1. Host Lava- petrography

The lava hosting the composite xenoliths is a pyroclastic calc-alkaline andesite (Sajona et al., 2000). The main mineral phases, plagioclase (36%), clinopyroxene (13%), orthopyroxene (<1%) and magnetite (<1%), are held within a glass matrix (51%).

Petrographic textures are shown in Figure 5.10. Figure 5.10a shows that the host andesite is a crystal rich, 2-pyroxene plagioclase pyroclastic deposit. Phenocrysts range in size and shape, many of which are broken. The andesite is quite vesicular, and much of the magnetite occurs within clinopyroxene phenocrysts (Figure 5.10b and c).

The andesite has had many recharge events and condition changes recorded in the phenocrysts. Resorption textures are seen in few large clinopyroxene phenocrysts (Figure 10e) and variably in plagioclase phenocrysts (Figure 5.10a and c). Many of the plagioclase phenocrysts have spongy cores with skeletal overgrowth (Figure 5.10 c "feld"). Interestingly, the location of the spongy texture is within the phenocryst varies. Furthermore, plagioclase phenocrysts records multiple magma recharge events seen in oscillatory zoning and inclusions forming rings along crystal growth planes (Figure 510f).

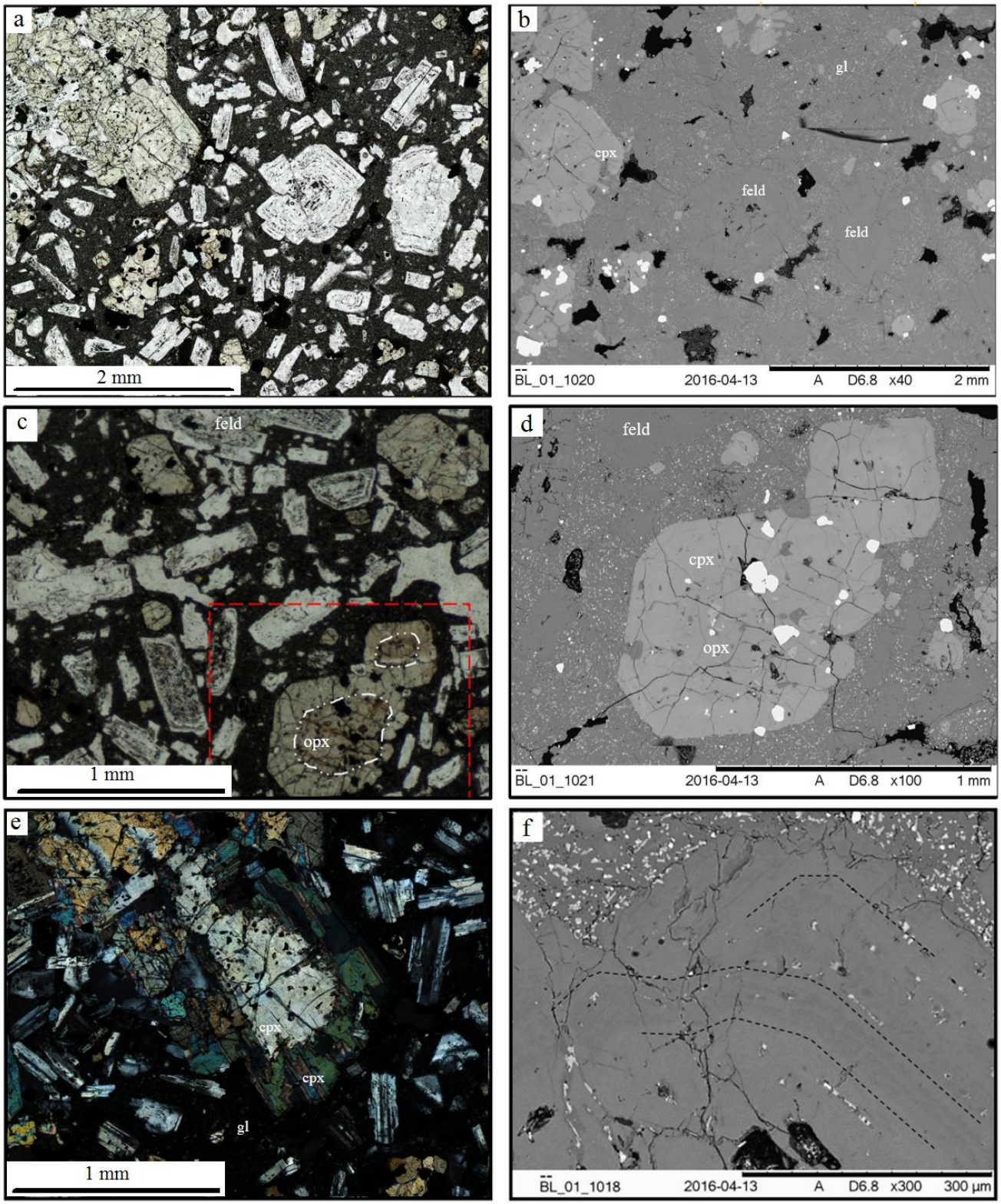

Figure 5.10: petrographic textures of the host andesite. a) PPL image showing variability of crystal form and size. b) BSE image of figure (a), magnetite is more easily identified. c) PPL image showing feldspar with spongy cores and skeletal overgrowth, as well as euhedral clinopyroxene with an orthopyroxene core. d) BSE image of the pyroxene phenocryst in (c). e) XPL image of a large clinopyroxene phenocryst with a relict resorbed core and skeletal overgrowth. f) BSE image of a plagioclase phenocryst with oscillatory zones highlighted.

Interestingly, the host andesite may have originally orthopyroxene saturated. None of the phenocrysts edges are orthopyroxene, and many of the euhedral clinopyroxene phenocrysts contain orthopyroxene cores (Figure 5.10c). The only occurrence of orthopyroxene in contact with the matrix is when the crystal have been broken during eruption.

Whilst the host andesite was plagioclase and 2-pyroxene saturated, it was never amphibole saturated. There are no phenocrysts of amphibole and no phenocrysts with amphibole cores overgrown by a mineral in equilibrium with the magma conditions.

5.4.2. Host Lava- major element chemistry

Representative analysis of major element point analyses of three mineral phases are the glass matrix are shown in Appendix 1, Tables 4 and 5.

Clinopyroxene is an augite composition (e.g. Morimoto et al., 1989) and highly variable (Figure 5.6e and f). Clinopyroxene $Mg_{\#}$ varies greatly ($Mg_{67.81\text{-}77.87}$) with no trend to this variation within individual clinopyroxene grains (i.e. core to rim) or with Ti (Figure 5.6e) which also shows variation (0.41-0.59 TiO_2). However, there is a negative linear relationship between $Mg_{\#}$ and Ca (Figure 5.6f), which varies considerably (18.62- 21.03 CaO). Importantly, clinopyroxene in the host andesite is chemically different to the clinopyroxene in the peridotite fragments.

Orthopyroxene in the host andesite is enstatitic (Morimoto et al., 1989). Compositions may vary, however few phenocrysts made analysis difficult. From the data collected, orthopyroxene in the host andesite has a much lower $Mg_{\#}$ ($Mg_{71.7}$) and higher Al_2O_3 (1.58 %) and MnO (0.48 %) compared to orthopyroxene from the peridotite fragments (Figure 5.6f).

Plagioclase phenocrysts in the host lava show much more major element variation than plagioclase in the composite xenolith. This variation is clearly represented in Figure 5.7b, as relative Ca-Na-K concentrations categorize the plagioclase as bytownite - labradorite in composition. Plagioclase is less calcic than anorthite feldspars from the xenolith, with $An_{\#}$ range from $An_{67.25\text{-}87.05}$. Variation is seen both between grains and within individual grains as well. $An_{\#}$ from core to rim vary from $An_{78.56 \rightarrow 87.01 \rightarrow 70.13}$. The variation in plagioclase phenocrysts is an order of magnitude larger than plagioclase within the xenolith.

The host matrix melt compositions are presented in Appendix 2, Table 6. The host andesite is not as silica rich as the melt inclusions within olivine. However, the matrix is more FeO (4.02%), Al_2O_3 (20.29)

and CaO (8.37) rich. There is still a strong alkali influence with high concentrations of Na_2O (4.83%) and K_2O (1.15%).

6. Interpretation

6.1. Significance of textural relationships in the xenolith

Petrographic and quantitative spatial analysis has been used to infer a four stage, relative geological history of the xenolith. A combined use of light microscopy, SEM EBSD and NT- Dingo analyses were needed to completely resolve each stage.

6.1.1. Stage 1- Deformed harzburgite.

The oldest component of the xenolith are the harzburgite fragments. They are numerous, irregularly shaped forming a large proportion of the xenolith (Figure5.1b and c- DINGO). The mineral assemblage within the fragments consists of olivine (~89%) and orthopyroxene (~11%) ± spinel. Olivine and orthopyroxene are the only phases that show significant internal deformation (Figure 5.2a and b). In contrast, the clinopyroxene and hornblende show no significant or systematic crystal plastic deformation.

Deformation features include undulose extinctions, kind bands (XPL, Figure 5.2) and sub-grain boundaries (EBSD, Figure 5.4). These are typical of crystal plastic deformation at high temperatures and medium strain rates, and commonly identified in mantle xenoliths from arc settings (e.g. Ionov, 2010; Ishimaru et al., 2007). They are dissimilar to the Ultra High Pressure (UHP) deformation experienced at the slab-mantle wedge boundary (e.g. Stöckhert and Wassman, 2013) or in shear zones (e.g. Bail and Trepmann, 2013), due to a lack of well-defined crystallographic preferred orientations or mylonitic grainsizes.

6.1.2. Stage 2- The reaction assemblage

The morphology of harzburgite nodules suggest the mantle wedge was brittle, and subsequently fractured, entrained by, and reacted with, a melt. Melt influx induced hydro-fracturing, and reaction occurred along the edges of the harzburgite fragments. NT3-Dimensional reconstructions give a strikingly clear indication that the nodules are completely encompassed by hornblendite in every case (Figure 5.1b and c).

Regardless of the hornblendite thickness, the harzburgite nodules are never in contact with the hornblende gabbro.

Hornblende and clinopyroxene are the mineral assemblage representing the melt-rock reaction. The textural relationship between clinopyroxene, hornblende and olivine are the same infiltration relationships at the peridotite-hornblendite contact (e.g. Figure 5.3a and c), and at the contact between single grain veinlets within the peridotite (Figure 5.2c and d). Regardless of locality, clinopyroxene and hornblende exploit the crystal lattice defects of olivine (Figure 5.4). Matching crystallographic orientations of olivine, and two relict olivines (Figure 5.4b) demonstrate that the propagation of hornblende encompassed multiple subgrains of olivine (e.g. Figure 5.2c). Furthermore, since adjacent clinopyroxene and hornblende occasionally have the same crystallographic orientation (Figure 5.4c), growth of the minerals were simultaneous and part of the same reaction:

Magma + Olivine = Amphibole ± Clinopyroxene.

This reaction driven, dissolution precipitation is similar to the process described by Ortoleva et al. (1987) and Szymczak and Ladd (2014). Figure 5.4b shows an incipient propagation of hornblende (point 4), thickening of a branch of hornblende (point 6) and the main body of hornblende (point 5) with matching crystallographic orientations. Thus because of this, the assumption is these three points link in a 3rd dimension to be one larger hornblende crystal. Accordingly, growth occurs fastest along the defects (point 4), which then propagates into the olivine perpendicular to the defect (point 6), and eventually encapsulates an olivine sub-grain (e.g. points 1 and 2). At one end of hornblende, growth is euhedral, at the other end, growth is defined by crystal lattice defects of olivine.

6.1.3. Stage 3- The hornblende gabbro.

The hornblendite and hornblende gabbro components of the xenoliths are in equilibrium with each other. The contact between the hornblendite and hornblende gabbro is defined by crystal shape and interlocking textures (Figure 5.5d). Thus demonstrates that crystallization of the anorthite in the gabbro was simultaneous at some stage of hornblende growth along the rim. Importantly, this is completely different to the infiltration relationship between olivine, hornblende and clinopyroxene (e.g. Figure 5.4).

Movement is shown by two petrographic features. Firstly, no particular harzburgite fragment has a preferred orientation relative to other fragments, suggesting they must have been rotated. This implies movement after fracturing (Figure 5.1b and c). Secondly, the finer grained hornblende gabbro (e.g. Figure

5.5a) also shows a flow texture. The gabbro must have been a crystalline mush as movement occurred as preferred orientations are found in axis 100 and 010 of hornblende and anorthite respectively (Figure 5.5c). Furthermore, the shape preferred orientation coexists with a lack of crystal plastic deformation (Figure 5.5c). Accordingly, the finer grainsize of the gabbro was not formed by sub-grain formation, but rather a high nucleation rate generated by flow. Since the melt was not able to react with olivine, crystallization of hornblende and anorthite must follow the following equation:

Magma → Hornblende + Anorthite.

Intriguingly, a particular textural feature in the gabbro not only suggests the melt entraining the harzburgite fragments stalled before moving as a composite. Annealing textures (e.g. 120°triple junctions) are commonly found in the gabbro (Figure 5.5b). This suggests the anorthite was able to equilibrate with the hornblende. Importantly, the 120°junctions are not deformed, suggesting annealing after the fluid stalled.

6.2.4. Stage 4- Host magma

The magma containing the xenoliths is an evolved, high K, calc-alkaline andesite (e.g. Arai et al., 1996; Sajona et al., 2000). Oscillatory zoning in plagioclase records many episodes of magma recharge (Figure 5.11d), suggesting an open system. Identification of spongy cores (i.e. re-sorption features) in some plagioclase crystals, and skeletal overgrowth, suggests the magma went through a decompression phase (Figure 5.6e). There was a point when the magma composition changed from orthopyroxene saturation to clinopyroxene saturation, as shown by the frequent orthopyroxene cores in clinopyroxene phenocrysts (Figure 5.6e).

Importantly, there is a lack of amphibole in the host lava, and textures in plagioclase from the host andesite differ from plagioclase in the gabbro. This, and the crystallographic preferred orientation of the plagioclase and hornblende (Figure 5.5c), suggests a separate magma sampled the composite. Importantly, the lack of breakdown features in hornblende (e.g. Rutherford and Hill, 1993) suggests eruption must have occurred rapidly after sampling of the conduit occurred.

6.2.5. Petrographic interpretation.

The multicomponent xenolith was formed as a result of the following sequence of events. The harzburgite - undergoing crystal plastic deformation - was brittle enough for an ascending melt to cause fracturing. Subsequently, a melt-rock reaction forming hornblendite rinds at the expense of olivine:

Melt + Olivine → Hornblende ± Clinopyroxene

The rind armors the fragments and slowing the dissolution – precipitation reaction. With the melt unable to react continue to react with olivine, crystallization of a cumulate gabbro followed:

Melt → Hornblende + Anorthite

resulting in a crystalline mush. Movement of this mush allowed the imprint of a shape preferred orientation and stalling of the magma allowed for plagioclase to equilibrate with amphibole (hence the 120° triple junctions). However equilibration of olivine did not occur. The result is harzburgite fragments always encompassed by a coarse grained hornblendite and then hornblende gabbro. Subsequently, a separate magma batch entrained the composite xenolith and ascended to a shallower andesitic magma chamber.

6.2. Geothermometry- further constraining physical conditions of origin

A number of experimentally derived geothermometers and geobarometers have been applied in order to constrain the P-T conditions under which the various components of the composite xenolith and its host lava formed.

6.2.1. P-T constraints for the peridotite fragments

As illustrated in Figure 6.1, a number of thermometers using adjacent clinopyroxene-orthopyroxene pairs suggest the peridotite fragments last equilibrated at temperatures of ~900-950 ºC. This is comparable to the ~920°C melt inclusion entrapment temperatures suggested by Schiano et al. (1995). Similar temperatures were suggested by Arai et al. (2004) based on two-pyroxene thermobarometry (950-990 °C using the thermometer of Wells (1977) or ~100 °C higher using the Wood and Banno (1973) thermometer). A pressure constraint of 0.49-0.53 GPa was obtained using Eqn 39 of Putirka (2008) and this is significantly

lower than the 1 GPa estimate of Arai et al. (2004) based on the coexistence of anorthite and olivine. However, this study has shown that anorthite is never found in contact with the harzburgite fragments (Figure 5.1b). Whilst the minerals in the fragments have a high Fe content and thermal re-equilibration may have occurred, a caveat to the calculations summarized in Figure 6.1, is that much of the clinopyroxene is secondary due to reaction between the harzburgite and sampling melt (Figure 5.4). Furthermore, K_d values between the pyroxene pairs suggest that they are not in equilibrium.

6.2.2. P-T conditions for the hornblendite rind.

There are two geothermometers that can be applied to the hornblendite rind: the formulation of Ridolfi et al. (2010); and the amphibole-plagioclase thermometer of Holland and Blundy (1994). The Ridolfi et al. (2010) geothermometer calculates crystallization at ~1000-1040 °C at 0.47-0.59 GPa (Figure 6.1a and b). Interestingly, this is slightly higher than temperatures calculated for the harzburgite fragments with much lower pressures than suggested by Arai et al. (2004). Assuming the pressure range of 0.47-0.59 GPa,

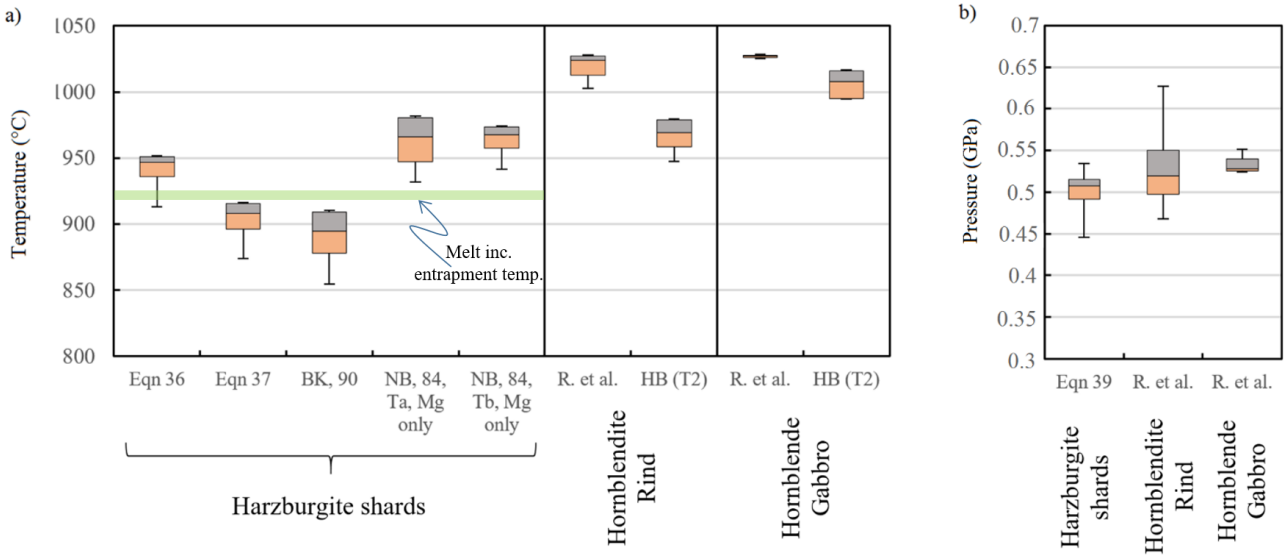

Figure 6.1: Box plot of P-T conditions for harzburgite fragments, hornblendite rind and hornblende gabbro. a) Calculated temperatures. Harzburgite temperatures calculated using 2-pyroxene thermometry, Eqn 36 and 37 from Putirka (2008). BK, 90 is Brey and Köhler (1990). NB, 84 is based on Mg abundance from Nickel and Brey (1984). Hornblendite rind and hornblende gabbro thermometry was calculated using Ridolfi et al. (2010) and Thermometer 2, Holland and Blundy (1994). Melt inclusion entrapment temperatures are ~920 °C (Schiano et al., 1995). b) Calculated pressure conditions. Harzburgite fragments using 2-pyroxene barometer from Putirka (2008). The hornblendite rind and hornblende gabbro pressures were calculated using Ridolfi et al. (2010).

plagioclase-amphibole pair thermometry calculates a temperature range of ~940-990 °C using Thermometer 2, Holland and Blundy (1994) (Figure 61a and b). Although major element variation in hornblende is due to melt-rock dissolution precipitation reactions, an interesting comparison between components can be made when the same thermometers are applied to the hornblende gabbro, which is not effected by reaction.

6.2.3. P-T constraints for the hornblende gabbro.

When applied to the gabbro, the formulation of Ridolfi et al. (2010) suggests temperatures of ~1020-1030 °C at 0.52-0.55 GPa (Figure 6.1a and b). This overlaps those obtained for the hornblendite. Interestingly, amphibole-plagioclase calculations (Holland and Blundy, 1994) suggest that the crystallization temperatures of the gabbro were slightly higher than the hornblendite rind (see Fig. 6.1a).

6.2.4. P-T constrains for the host lava.

Thermobarometry of the host lava is illustrated in Figure 6.2. Calculated clinopyroxene-glass temperatures are ~1050-1150 °C (Figure 6.2a), which is comparable to the Lindsley, (1983) 5 kbar 1000-1100 °C contours (Figure 6.2c). These temperatures are comparable to experimental estimates of eruption temperatures of Japanese andesites similar to the host andesite (Sekine et al., 1979). Sisson and Grove (1993), show low MgO (<5 wt.%) and high Al basaltic andesites, like the host andesite, erupt at similar temperatures (~1100 °C). Whilst caution needs to be taken with the small variation, multiple thermometers consistently calculate higher temperatures then those calculate for the hornblendite and hornblende gabbro. Importantly, these temperatures are also the upper limit of amphibole stability (e.g. Green, 1992).

Clinopyroxene-glass barometry (e.g. Putirka, 2008) records pressure conditions (0.22-0.38 GPa, Figure 6.2b) immediately before eruption. Interestingly, host lava matrix liquid equilibria sits relatively close to the low pressure cotectic (Figure 6.2d).

6.2.5. P-T interpretation.

The P-T conditions at which the harzburgite last equilibrated were ~ 900-950 ºC at 0.5 GPa. Likely geotherms would place these conditions within the sub-arc lithosphere (see Fig. 2b of Turner et al., 2011).

This is consistent with the fragment-like morphology of the harzburgite which suggests that they were entrained as brittle fragments potentially broken off the walls of a magma conduit. The magma that picked these up had a temperature which did not exceed ~1050 °C and formed hornblende by reacting with the peridotite fragments at ~1000 ºC. Subsequently the magma crystallized a plagioclase-amphibole gabbro cumulate around the nodule. All of this occurred at ~ 0.5 GPa within the sub-arc lithosphere where the magma was saturated in amphibole. The host andesite magma chamber ~8 km beneath Batan Island (1050-1100 °C at 0.25-0.30 GPa) is within the lithospheric crust. This probably corresponds to the depth of vapor (H_2O) saturation (e.g. Adam et al., 2016a).

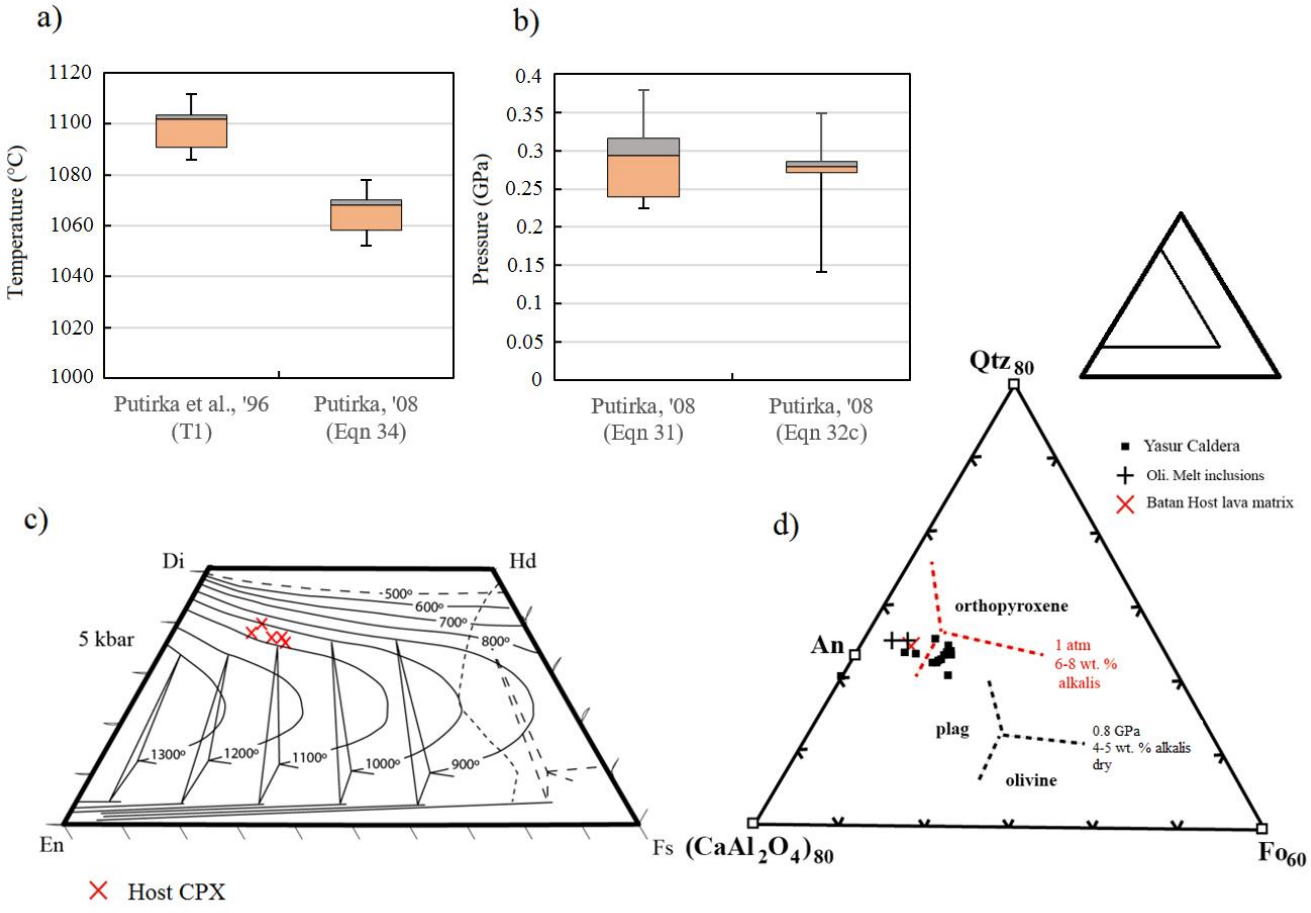

Figure 6.2: Calculated P-T conditions for the host lava from major element data. a) Calculated temperatures using clinopyroxene-Glass calculations (Putirka et al., 1996, T1; Putirka, 2008, Eqn 34). b) Calculated pressure conditions using clinopyroxene-glass barometry from Putirka (2008, Eqn 31 and 32c). c) clinopyroxene compositions plotted on an En-Wo-Fs ternary, the 5 kbar temperature contour from Lindsley (1983). d) Glass compositions plotted on a nepheline-quartz-forsterite liquid equilibria ternary from Adam et al. (2016b).

6.3. Insights from trace element data

Trace element abundances in the minerals from each xenolith component have been used to further constrain the magmatic processes occurring beneath Batan Island.

6.3.1. Chemical evidence for nature and origin of the harzburgite fragments.

Previous studies have inferred the mantle wedge beneath Batan Island to be heavily metasomatised depleted mantle (e.g. Maury et al., 1992; Defant et al., 1990). Maury et al. (1992) were the first to observe that xenoliths entrained in the youngest phase of volcanics from Mt. Iraya volcano have an arc-like trace element signature. That is, a relative enrichment in elements like Rb, Ba, Th, U, and La compared to Nb, Ta, Zr, Hf, Ti and the HREE's (e.g. Yb and Lu). The inference is that the mantle beneath Batan Island has been strongly influence by slab and sediment melts (e.g. Maury et al., 1992; Schiano et al., 1995; Fourcade et al., 1994) and that this occurred relatively recently (e.g. Turner et al., 2012).

The same trace element signatures have been identified in this study. Olivine and orthopyroxene trace element abundances are unlike those expected from a depleted mantle signature (Figure 5.8). Olivine trace element abundances show arc-like signatures (Figure 5.8a), similar to those from olivine separates containing adakitic melt inclusions analyzed by Schiano et al. (1995). The same melt inclusions have been identified in the harzburgite fragments analyzed here (Figure 5.2f). Furthermore, the trace element signature of the melt inclusions (Schiano et al., 1995) are very similar to that the olivine in this study (Figure 6.3). This demonstrates how the slab and sediment derived fluids have metasomatised the harzburgite, altering the trace element signature to no longer reflect the depleted mantle and without any change to the mineral assemblage.

6.3.2. Linking the reaction assemblage to the hornblende gabbro.

Incompatible trace element signatures of hornblende are relatively uniform, regardless of the location within the xenolith (Figure 5.9). Whilst the major element compositions vary due to different crystallization conditions (i.e. melt-rock reaction or cumulate crystallization) (Figure 5.6a and b), the trace element signatures all have positive anomalies in Ba and Sr, and negative anomalies in Th, U, Zr, K and Pb. The calculated equilibrium melt compositions demonstrates that the hornblendes, whether crystallized by

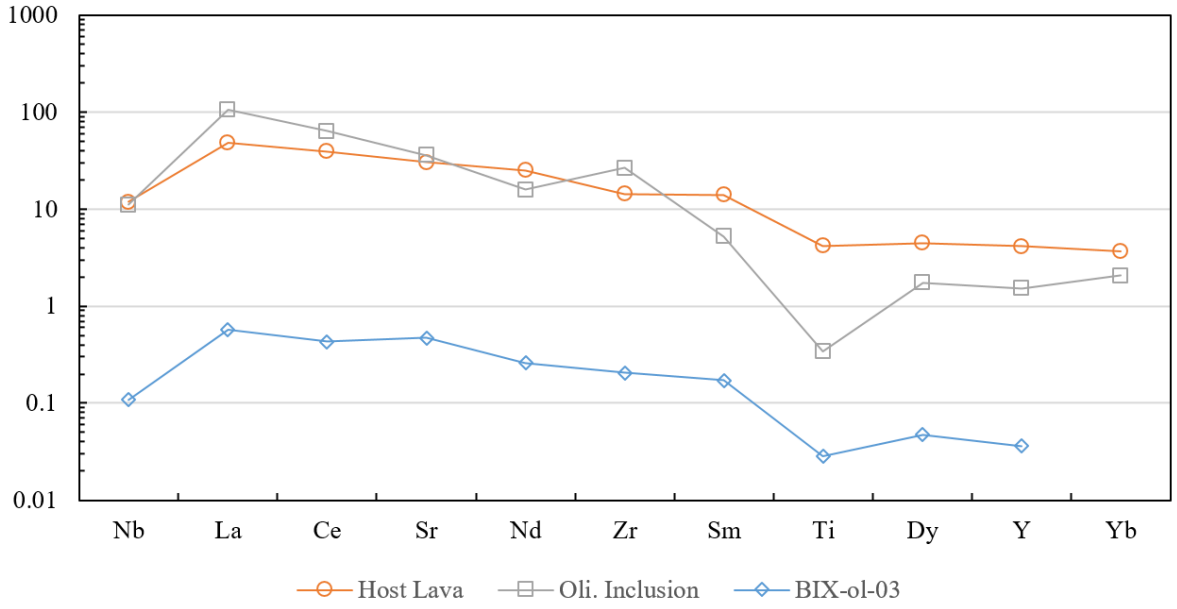

Figure 6.3: REE + Ti patterns for the Host Lava (Turner et al., 2012), the adakitic melt inclusion in olivine (Schiano et al., 1995), and olivine. Normalised to Primitive Mantle (McDonough and Sun, 1995).

reaction or as a cumulate, were in equilibrium with (i.e. crystallized from) the same melt (Figure 5.8b). Furthermore, the similarity of the equilibrium melt compositions for hornblende and clinopyroxene (Figure 5.8c) suggest that hornblende and clinopyroxene in the harzburgite fragments formed as part of the same reaction between melt and olivine.

Interestingly, the equilibrium melt composition of orthopyroxene is remarkably similar to hornblende and clinopyroxene (Figure 5.8d). The only difference is the inversion of the negative Pb anomaly in the clinopyroxene (Figure 5.8c). Since clinopyroxene and orthopyroxene are often adjacent crystals, it is possible that Pb preferentially partitions into orthopyroxene in these reaction circumstances.

6.3.3. The link between olivine, equilibrium melt, and host andesite.

As shown in Figure 6.3, the REE patterns of olivine and the host andesite are nearly identical. This striking correlation was first shown by Maury et al. (1992), comparing whole rock xenolith and host andesite data (see Fig. 1c of Maury et al.). Furthermore, they estimated that 3% melting of the mantle xenolith would produce the abundances observed in the host andesite.

The host andesite signature shows a general enrichment in LREE's over HREE's (Figure 5.8b-d) Negative anomalies in Ba, Nb, K and Ti, mirrored by the calculated equilibrium melt compositions for hornblende (5.8b), clinopyroxene (5.8c), orthopyroxene (5.8d).

Two important links can be made: (1) the melt transporting the harzburgite fragments must be of mantle origin; and (2) the melt transporting the harzburgite fragments could be the same magma because trace element signatures of olivine and the host andesite are identical,. Therefore, the crystallization of amphibole can be the evolution pathway fractionating a basaltic melt (e.g. olivine- mantle origin) into an evolved melt (e.g. host andesite).

6.3.4. Trace element interpretation.

The mantle wedge beneath contains a high level of metasomatism by slab and sediment derived components (e.g. Maury et al., 1992; Schiano et al., 1995; Fourcade et al., 1994, Turner et al., 2012). Importantly, trace element signatures demonstrate the both melt-rock reaction, and cumulate (gabbro) crystallization were imparted from the same melt of mantle origin.

Interestingly, the incompatible element signatures of the sampling magma and host andesite appear nearly identical. It is possible they are the same melt. If this were the case, hornblende would be a phenocryst phase in, or at least a relict within, the host lava. The conundrum is why amphibole is not a phenocryst phase in the host andesite.

7. Petrogenic Model: Combining petrographic and geochemical interpretations

In this section the new findings of this study are placed in the context of prior work. The results provide important constraints on the questions surrounding xenolith formation, the importance of amphibole in arc settings and implications for arc volcanism.

7.1. Xenolith Formation

As illustrated in Figure 7.1, the following sequence of events described the xenoliths history through to eruption.

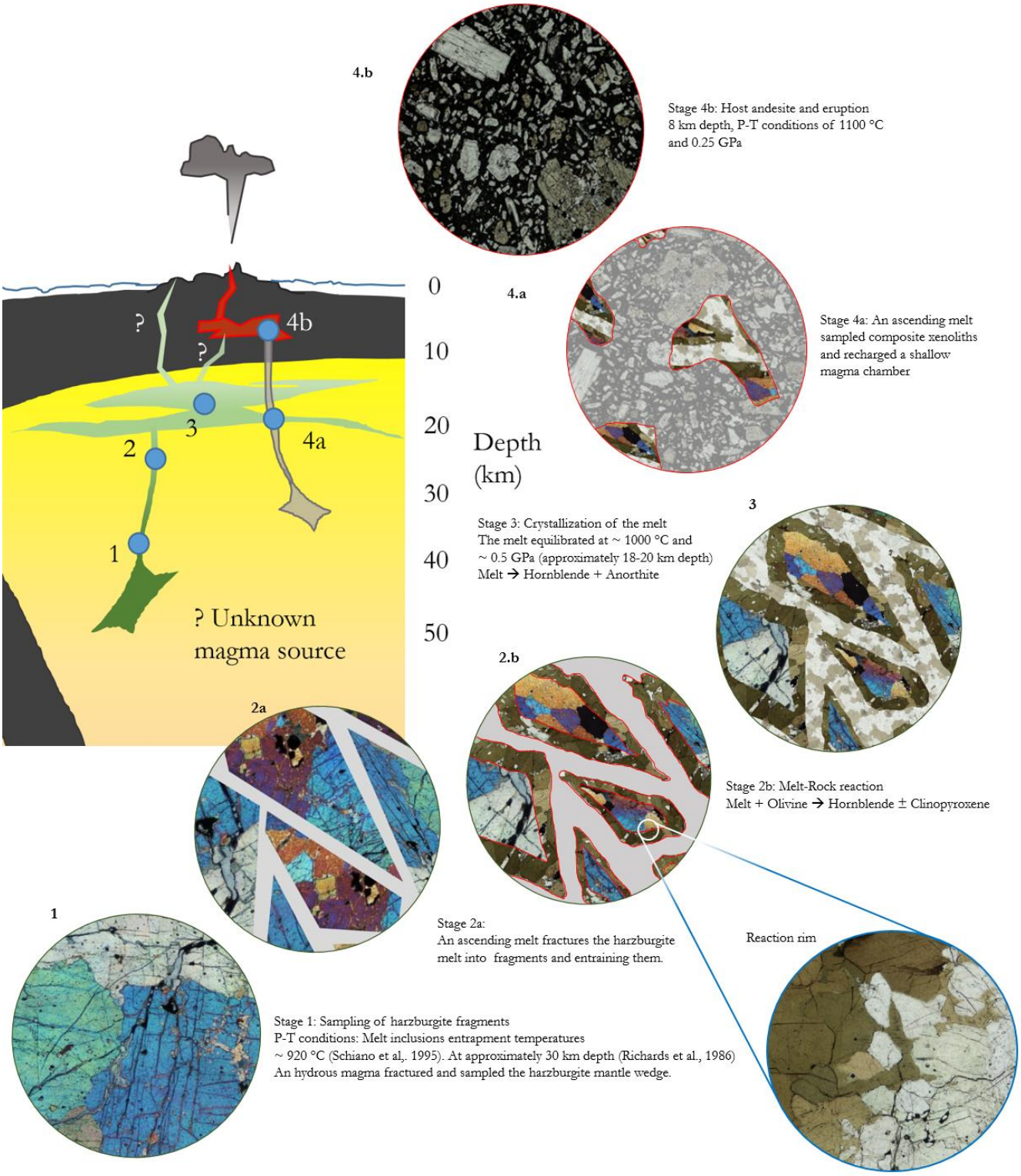

Figure 7.1. Schematic linking the entire process from sampling the harzburgite to eruption. The schematic represents the mantle directly beneath Batan Island. Note: The tectonic structure and photomicrographs are not to scale, the depths (in km) are to a relative scale.

Stage 1. Harzburgite

The mantle wedge under Batan Island was initially depleted mantle and subsequently metasomatised (e.g. Maury et al., 1992). The sampled section of the mantle has lost a melt fraction and adakitic melt inclusions record entrapment record temperatures ~920 °C (Schiano et al., 1995; Figure 6.1a). Importantly, the highly metasomatised nature of the fragments (~Fo80) suggests interaction with slab-derived fluids and thermal re-equilibration. Interestingly, crystal plastic deformation is still prevalent and the lack garnet provides an upper limit of pressure of 1.2 GPa (Alonso-Perez et al., 2009). The thermobarometry suggests the sampled fragments are of relatively shallow origin in the sub-arc lithosphere (~30 km, Richards et al., 1986) yet nonetheless provide analogues of the mantle wedge (Maury et al., 1992).

Stage 2a. Fracturing and entrainment

An ascending basaltic magma caused fracturing and entrained the harzburgite mantle as fragments. Whilst the fragments are not a direct sample of the source region of the melt, links between olivine and calculated equilibrium melt compositions suggest that the melt is of mantle origin- not slab derived. Furthermore, did not originate from depths where garnet is stable. REE patterns do not show the strong depletions in HREE's that would be expected by residual garnet (Davidson et al., 2013).

Stage 2b. Melt-Rock reaction

The ascending hydrous, alkali rich, amphibole saturated magma entrained the fragments at the upper temperature limits of amphibole stability (~1000 °C; e.g. Foden and Green, 1992). Immediate reactions along the fractured edges of the harzburgite fragments follow reaction (1). The dissolution precipitation reaction, exploiting crystal lattice defects, armors the fragments in hornblendite and slows further reaction.

$$\text{Melt} + \text{Olivine} \rightarrow \text{Hornblende} \pm \text{Clinopyroxene} \quad (1)$$

Stage 3. Crystallization of the melt

The hornblende rind subsequently acts as barrier between the melt and olivine (Figure 5.1). Accordingly, once olivine is removed, the melt can no longer react with olivine and follows equation (2).

$$\text{Melt} \rightarrow \text{Hornblende} + \text{Anorthite} \quad (2)$$

The melt equilibrated at ~1000 °C and 0.5 GPa crystallized a cumulate assemblage of hornblende and plagioclase. These conditions roughly correspond to those just beneath the oceanic crust at appoximately18-20 km depth (e.g. Dimalanta and Yumul, 2003). Importantly, the temperatures are within the upper limits of amphibole P-T stability for basaltic-andesitic magma (e.g. Allan and Boettcher, 1983;

Foden and Green, 1992; Green, 1992). The result is a crystallized, composite conduit with harzburgite fragments encased in a hornblendite rind and then hornblende gabbro.

Stage 4a. Sampling the composite conduit

A new ascending magma then sampled the composite xenoliths in the conduit and continued to rise and recharge a shallow magma chamber. Evidence for this is the difference in temperatures between the xenolith and the host andesite. The resulting thermal dis-equilibrium would ultimately result in dissolution of the xenolith. Thus, the survival of the xenolith and the lack of hornblende breakdown features demand a fast ascent rate and eruption within days of entrainment (Brearley and Scarfe, 1986; Rutherford and Hill, 1993). Conversely, this timeframe would not allow for the growth of the phenocrysts observed in the host andesite.

Stage 4b. Host andesite and eruption

The lava residing in the shallow magma chamber was an evolved, crystal rich, high K calc-alkaline andesite. The P-T conditions of this chamber were ~1100 °C at ~0.25 GPa. These temperatures are above the upper extremes of amphibole stability (e.g. Foden and Green, 1992; Green, 1992). Thus, the host andesite was saturated in two pyroxenes and plagioclase, but not amphibole.

After eruption, the final product is a composite xenolith of deformed harzburgite fragments, surrounded by a reaction rind and then hornblende gabbro, entrained in a plagioclase rich, two pyroxene host andesite.

7.2. Amphibole fractionation in arc settings

Davidson et al. (2007 and 2013) suggest amphibole must be a major mineral in the petrogenesis, and evolution, of arc lavas. Relative concentrations of La, Dy and Yb can, in principle, provide a simple indication of whether differentiation was dominated by clinopyroxene, garnet or amphibole (Figure 7.2a). Interestingly, published trace element data from many arc settings supports the notion that amphibole fractionation occurs frequently (Figure 7.2b; Davidson et al., 2013). What is surprising is that many of the lavas in arc settings are amphibole free.

The same situation occurs at Batan Island. Published trace element data on the lavas from Batan Island (e.g. McDermott et al., 1993) clearly suggests that amphibole fractionation is important (Figure 7.2b). Although some andesites on Batan Island are amphibole rich (Sajona et al., 2000), the presence of amphibole

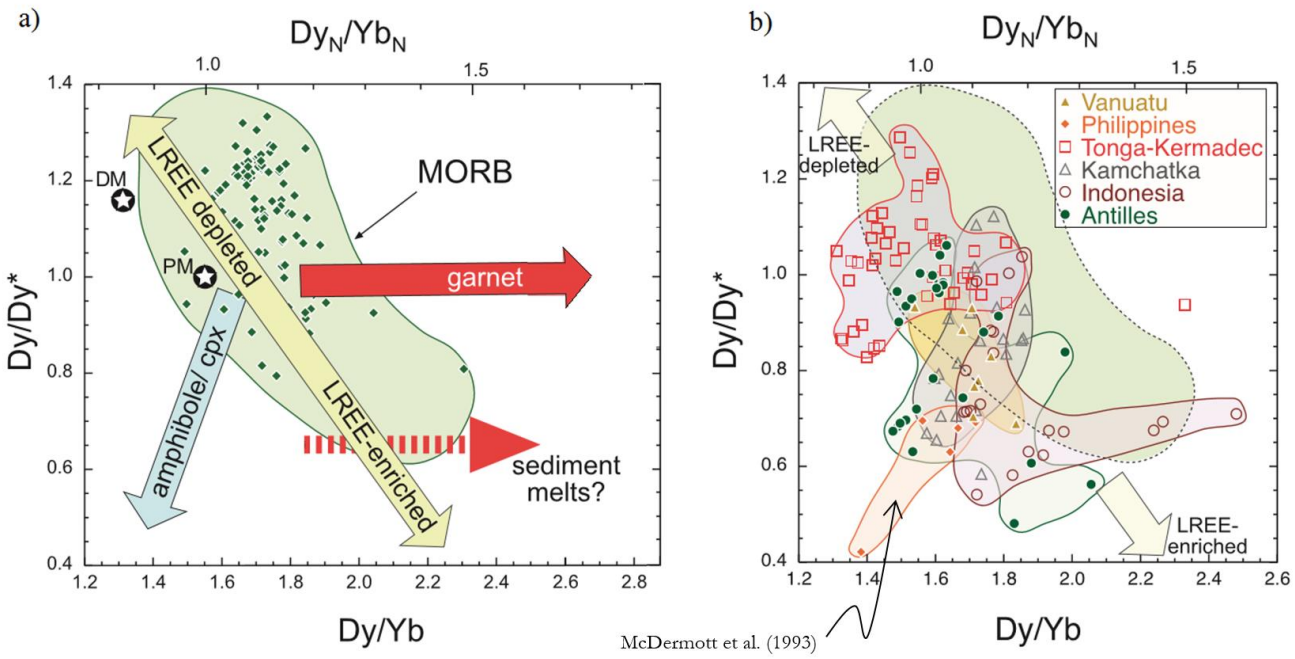

Figure 7.2: Plot of Dy/Dy* versus Dy/Yb where Dy/Dy* = $\frac{Dy_n}{La_n^{4/13} \times Yb_n^{9/13}}$ where n is chondrite normalized, from Davidson et al. (2013). a) Highlights mineral fractionation direction relative to proportions of Dy, La and Yb. b) Trace element data from several arc settings, the majority suggesting amphibole fractionation. Philippine data from McDermott et al. (1993).

rich xenoliths in an amphibole free host lava provide important corroborating evidence that this phase was important in the petrogenesis of the lavas.

7.3. Batan Island volcanism

The findings in this study provide some interesting insights into the volcanic processes occurring beneath Batan Island. The unique composite xenolith clearly shows that amphibole was stable at some point time, and importantly both during melt-wall rock reaction and cumulate crystallization at 0.5 GPa. This alone demonstrates that amphibole fractionation is occurring under Batan Island, and may occur in other arc settings.

Furthermore, there are several other lavas which have hornblende as an abundant phenocryst phase on Batan Island (Sajona et al., 2000). These hornblende andesites have adakitic compositions, and whilst nearly 1 Ma separates the eruptions, why amphibole was stable in the older lavas and not the younger ones may provide important insights into changes in the evolutionary path of the magmas through time.

8. Conclusions

Existing literature on these composite xenoliths only focus on the harzburgite nodules. Recent metasomatism (Turner et al., 2012), by fluids with slab and sediment components has given the mantle beneath Batan Island an 'arc-like' signature (e.g. Maury et al., 1992; Schiano et al., 1995; Fourcade et al., 1994; Vidal et al., 1989). Only select work has mentioned the amphibole rind and amphibole gabbro as xenolith components (e.g. Arai and Kida, 2000; Arai et al., 2004). This study focuses on the entire composite xenolith, applying Neutron Tomography as a novel technique, alongside the more conventional methods, such as SEM EBSD, EMP major element and LA-ICP-MS trace element analyses, to make the following conclusions.

(1) The multicomponent xenolith formed in the following sequence of events. (A) An ascending melt of shallow mantle origin fractured and entrained harzburgite fragments, (B) and reacted to crystallize a rind of hornblende at the expense of olivine and slowing reaction. (C) The melt then crystallized hornblende and anorthite, equilibrating at ~0.5 GPa and ~1000 °C. The crystallized conduit did not reach the host andesite magma chamber. (D) A separate magma sampled the composite xenolith, transporting it to the host andesite magma chamber at ~0.25 GPa and ~1100 °C. (E) Eruption must have been recent due to the survival of the xenolith in a magma it was out of equilibrium with.

(2) Amphibole is stable at conditions beneath Batan Island. Wall-rock reactions and cumulate growth demonstrates that mass crystallization of amphibole can act as a fractionation event as suggested to occur by Davidson et al. (2007 and 2013). Several volcanic events on Batan Island contained amphibole as a phenocryst phase (Sajona et al., 2000). Potentially, the magma (or those similar) forming the hornblendite rind and then gabbro could have reached the surface. Notwithstanding, studies would need to show links between amphiboles in xenoliths, and amphiboles and the host magma.

(3) Amphibole crystallized under multiple conditions beneath Batan Island. Thus, the processes described to form these composite xenoliths can be used as an analogue for other arc settings which show evidence for amphibole fractionation.

References

Abe N., Arai S. and Yurimoto H., (1998), Geochemical characteristics of the uppermost mantle beneath the Japan island arcs: implications for upper mantle evolution, *Physics of the Earth and Planetary Interiors*, 107: 233-248.

Adam J. and Green T., (2006), Trace element partitioning between mica- and amphibole-bearing garnet lherzolite and hydrous basanitic melt: 1. Experimental results and the investigation of controls on partitioning behavior, *Contributions to Mineralogy and Petrology*, 152: 1-17.

Adam J., Turner M., Hauri E.H. and Turner S., (2016a), Crystal/melt partitioning of water and other volatiles during the near-solidus melting of mantle peridotite: comparisons with non-volatile incompatible elements and implications for the generation of intraplate magmatism, *American Mineralogist*, 101(4): 876-888.

Adam J., Turner S. and Rushmer T., (2016b), The genesis of silicic arc magmas in shallow crustal cold zones, *Lithos*, 264: 472-494.

Allen J.C. and Boettcher A.L., (1983), The stability of amphibole in andesite and basalt at high pressures, *American Mineralogist*, 68: 307-314.

Alonso-Perez R., Müntener O., Ulmer P., (2009), Igneous garnet and amphibole fractionation in the roots of island arcs: experimental constraints on andesitic liquids, *Contributions to Mineralogy and Petrology*, 157: 541-558.

Anderson A.T. Jr., (1980), Significance of hornblende in calc-alkaline andesites and basalts, *American Mineralogist*, 65: 837-851.

Arai S. and Ishimaru S., (2008), Insights into Petrological Characteristics of the Lithosphere of Mantle Wedge beneath Arcs through Peridotite Xenoliths: a Review, *Journal of Petrology*, 49(4): 665-695.

Arai S. and Kida M., (2000), Origin of fine-grained peridotite xenoliths from Iraya volcano of Batan Island, Philippines: deserpentinization or metasomatism at the wedge mantle beneath an incipient arc?, *The Island Arc*, 9: 458-471.

Arai S., Kida M., Abe N., Ninomiya A., Yumul G.P., (1996), Classification of peridotite xenoliths in calc-alkaline andesite form Iraya volcano, Batan Island, the Philippines, and its genetical implications, *Science Reports of the Kanazawa University*, 41(1): 25-45.

Arai S., Takada S., Michibayashi K. and Kida M., (2004), Petrology of Peridotite Xenoliths from Iraya Volcano, Philippines, and its Implication for Dynamic Mantle-Wedge Processes, *Journal of Petrology*, 45(2): 369-389.

Arculus R.J. and Wills K.J.A., (1980), The petrology of plutonic blocks and inclusions form the Lesser Antilles Island Arc, *Journal of Petrology*, 21(4): 743-799.

Bénard A. and Ionov D.A., (2013), Melt- and Fluid-Rock Interaction in Supra-Subduction Lithospheric Mantle: Evidence from Andesite-hosted Veined Peridotite Xenoliths, *Journal of Petrology*, 54(11): 2339-2378.

Bail J., and Trepmann C.A., (2013), The microstructural record of porphyroclasts and matrix of partly serpentinized peridotite mylonites- from brittle and crystal-plastic deformation to dissolution-precipitation creep, *Solid Earth*, 4: 315-330.

Blundy J.D. and Holland T.J.B., (1990), Calcic amphibole equilibria and a new amphibole-plagioclase geothermometer, *Contributions to Mineralogy and Petrology*, 104: 208-224.

Bons P.D. and den Brok B., (2000), Crystallographic preferred orientation development by dissolution-precipitation creep, *Journal of Structural Geology*, 22: 1713-1722.

Brearley M. and Scarfe C.M., (1986), Dissolution Rates of Upper Mantle Minerals in an Alkali Basalt Melt at High Pressure: An Experimental Study and Implications for Ultramafic Xenolith Survival, *Journal of Petrology*, 27: 1157-1182.

Brey G.P. and Köhler T., (1990), Geothermobarometry in Four-phase Lherzolites II. New Thermobarometers, and Practival Assessment of Existing Thermobarometers, *Journal of Petrology*, 31(6): 1353-1378.

Chadam J., Hoff D., Merino E., Ortoleva P. and Sen A., (1986), Reactive Infiltration Instabilities, *IMA Journal of Applied Mathematics*, 36: 207-221.

Davidson J., Turner S., Handley H., Macpherson C. and Dosseto A., (2007), Amphibole "sponge" in arc crust?, *Geology*, 35(9): 787-790.

Davidson J., Tuner S. and Plank T., (2013), Dy/Dy*: Variations Arising from Mantle Sources and Petrogenetis Processes, *Journal of Petrology*, 54(3): 525-537.

Debari S., Kay S.M. and Kay R.W., (1987), Ultramafic Xenoliths from Adagdak Volcano, Adak, Aleutian Islands, Alaska: Deformed Igneous Cumulates from the Moho of an Island Arc, *The Journal of Geology*, 95(3): 329-341.

Deer W.A., Howie R.A. and Zussman J., (1992), An Introduction to the Rock-Forming Minerals, 2nd Edition, *Pearson Education Limited*, England.

Defant M.J., Maury R.C., Joron J.L., Feigenson M.D., Leterrier J., Bellon H., Jacques D. and Richard M., (1990), The geochemistry and tectonic setting of the northern section of the Luzon arc (the Philippines and Taiwan), *Tectonophysics*, 183: 187-205.

Dimalanta C.B. and Yumul G.P. Jr., (2003), Magmatic and Amagmatic Contributions to Crustal Growth of an Island-Arc System: The Philippine Example, *International Geology Review*, 45: 922-935.

El-Rahman Y.A., Helmy H.M., Shibata T., Yoshikawa M., Arai S. and Tamura A., (2012), Mineral chemistry of the Neoproterozoic Alaskan-type Akarem Intrusion with special emphasis on amphibole: Implication for the pluton origin and evolution of subduction related magma, *Lithos*, 155: 410-425.

Foden J.D. and Green D.H., (1992), Possible role of amphibole in the origin of andesite: some experimental and natural evidence, *Contributions of Mineralogy and Petrology*, 109: 479-493.

Fourcade S., Maury R.C., Defant M.J. and McDermott F., (1994), Mantle metasomatic enrichment versus arc crust contamination in the Philippines: Oxygen isotope study of Batan ultramafic nodules and northern Luzon arc lavas, *Chemical Geology*, 114: 199-215.

Franz L., Becker K.P., Kramer W. and Herzig P.M., (2002) Ultramafic Xenoliths from Adagdak Volcano, Adak, Aleutian Islands, Alaska: Deformed Igneous Cumulates from the Moho of an Island Arc, *Journal of Petrology*, 43(2): 315-343.

Gerya T.V. and Stöckhert B., (2002), Exhumation rates of high pressure metamorphic rocks in subduction channels: The effect of Rheology, *Geophysical Research Letters*, 29(8): 1261-1264.

Green T.H., (1992), Experimental phase equilibrium studies of garnet-bearing I-type volcanics and high-level intrusives from Northland, New Zealand, *Transactions of the Royal Society of Edinburgh: Earth Sciences*, 83: 429-438.

Grégoire M., Jégo S., Maury R., Payot B.D., Tamayo R.A. and Yumul G.P., Metasomatic interactions between slab-derived melts and depleted mantle: Insights from xenoliths within Monglo adakite (Luzon arc, Philippines), *Lithos*, Elsevier, (2008), 103(3-4): 415-430.

Grégoire M., McInnes B.I.A. and O'Reilly S., (2001), Hydrous metasomatism of oceanic sub-arc mantle, Lihir, Papua New Guinea, Part 2. Trace element characteristics of slab-derived fluids, *Lithos*, 59: 91-108.

Halama R., Savov I.P., Rudnick R.L. and McDonough W.F., (2009), Insights into Li and Li isotope cycling and sub-arc metasomatism from veined mantle xenoliths, Kamchatka, *Contributions to Mineralogy and Petrology*, 158: 197-222.

Holland T. and Blundy J., (1994), Non-ideal interactions in calcic amphiboles and their bearing on amphibole-plagioclase thermometry, *Contributions to Mineralogy and Petrology*, 116: 433-447.

Imon R., Okudaira T. and Kanagawa K., (2004), Development of shape- and lattice- preferred orientations of amphibole grains during initial clastic deformation and subsequent deformation by dissolution-precipitation creep in amphibolites from the Ryoke metamorphic belt, SW Japan, *Journal of Structural Geology*, 793-805.

Ionov D.A., (2010), Petrology of Mantle Wedge Lithosphere: New Data on Supra-Subduction Zone Peridotite Xenoliths from the Andesitic Avacha Volcano, Kamchatka, *Journal of Petrology*, 51(1&2): 327-361.

Ionov D.A. and Seitz H.M., (2008), Lithium abundances and isotopic compositions in mantle xenoliths from subduction and intra-plate settings: Mantle sources vs. erupted histories, *Earth and Planetary Science Letters*, 266: 316-331.

Ishimaru S., Arai S., Ishida Y., Shirasaka M. and Okrugin C.M., (2007), Melting and Multi-stage Metasomatism in the Mantle Wedge beneath a Frontal Arc Inferred from Highly Depleted Peridotite Xenoliths from the Avacha Volcano, Southern Kamchatka, *Journal of Petrology*, 48(2) 395-433.

Klügel A., (1998), Reactions between mantle xenoliths and host magma beneath La Palma (Canary Islands): constrains on magma ascent rates and crustal reservoirs, *Contributions to Mineralogy and Petrology*, 131: 237-257.

Leake B.E., Woolley A.R., Arps C.E.S., Birch W.D., Gilbert M.C., Grice J.D., Hawthorne F.C., Kato A., Kisch H.J., Krivovichev C.G., Linthout K., Laird J., Mandarino J.A., Maresch W.V., Nickel E.H., Rock N.M.S., Schumacher J.C., Smith D.C., Stephenson N.C.N., Ungaretti L., Whittaker E.J.W. and Youzhi G., (1997), Nanomenclature of amphiboles: Report of the subcommittee on amphiboles of the International Mineralogical Association, commission of new minerals and mineral names, *The Canadian Mineralogist*, 35: 219-246.

Le Roux V., Dick H.J.B. and Shimizu N., (2014), Tracking flux melting and melt percolation in supra-subduction peridotites (Josephine ophiolite, USA), *Contributions to Mineralogy and Petrology*, 168: 1064-1085.

Liang Y. and Guo Y, (2003), Reactive dissolution instability driven by chemical diffusion with applications to harzburgite reactive dissolution, *Geophysical Research Letters*, 30(13) 1722-1725.

Lindsley D.H., (1983), Pyroxene thermometry, *American Mineralogist*, 68: 477-493.

Maury R.C., Defant M.J. and Joron J.L., (1992), Metasomatism of the sub-arc mantle inferred from trace elements in Philippine xenoliths, *Letters to Nature*, 360: 661-663.

McDermott F., Defant M.J., Hawkesworth C.J., Maury R.C. and Joron J.L., (1993), Isotope and trace element evidence for three component mixing in the genesis of the North Luzon arc lavas (Philippines), *Contributions to Mineralogy and Petrology*, 113: 9-23.

McDonough W.F. and Sun S.-s., (1995), The composition of the Earth, *Chemical Geology*, 120: 223-253.

McInnes B.I.A., Grégoire M., Binns R.A., Herzig P.M. and Hannington M.D., (2001), Hydrous metasomatism of oceanic sub-arc mantle, Lihir, Papua New Guinea: petrology and geochemistry of fluid-metasomatised mantle wedge xenoliths, *Earth and Planetary Science Letters*, 188: 169-183.

Morimoto N., Fabries J., Ferguson A.K., Ginzburg I.V., Ross M., Seifert F.A., Zussman J., Aoki K. and Gottardi G., (1989), Nomenclature of pyroxenes, *Mineralogical Journal*, 14(5): 198-221.

Neal C.R., (1988), The Origin and Composition of Metasomatic Fluids and Amphiboles beneath Malaita, Solomon Islands, *Journal of Petrology*, 29(1): 149-179.

Nixon P.H., (1987), Mantle Xenoliths, Wiley Interscience Publications, John Wiley & Sons. Chichester.

Ortoleva P., Chadam J., Merino E. and Sen A., (1987), Geochemical self-organization II: The reactive-infiltration instability, *American Journal of Science*, 287: 1008-1040.

Parkinson I.J., Arculus R.J. and Eggins S.M., (2003), Peridotite xenoliths from Grenada, Lesser Antilles Island Arc, *Contributions to Mineralogy and Petrology*, 146: 241-262.

Prouteau G., Scaillet B., Pichavant M. and Maury R., (2001), Evidence for mantle metasomatism by hydrous silicic melts derived from subducted oceanic crust, *Letters to Nature*, 410: 197-200.

Putirka K.D., (2008) Thermometers and barometers for Volcanic Systems, Chapter 3 in, Minerals, Inclusions and Volcanic Processes, Reviews in Mineralogy and Geochemistry, 69(1): 61-120.

Richard M., Maury R.C., Bellon H., Stephan J.-F., Boirat J.-M. and Calderon A., (1986), Geology of Mt Iraya volcano and Batan Island, northern Philippines, *Bulletin of Volcanology*, 3: 1-27.

Ridolfi F., Renzulli A., Puerini M., (2010), Stability and chemical equilibrium of amphibole in calc-alkaline magmas: an overview, new thermobarometric formulations and application to subduction-related volcanoes, *Contributions to Mineralogy and Petrology*, 160: 45-66.

Rutherford M.J. and Hill P.M., (1993), Magma ascent rates from amphibole breakdown: An experimental study applied to the 1980-1986 Mount St. Helens eruptions, *Journal of Geophysical Research*, 98(B11): 19,667-19,685.

Sajona F.G., Maury R.C., Prouteau G., Cotton J., Schiano P., Bellon H. and Fontaine L., (2000), Slab melt as metasomatic agent in island arc magma mantle sources, Negros and Batan (Philippines), *The Island Arc*, 9: 472-486.

Schiano P., Clocchiatti R., Shimizu N., Maury R.C., Jochum K.P. and Hofmann A.W., (1995), Hydrous, silica-rich melts in the sub-arc mantle and their relationship with erupted arc lavas, *Nature*, 377(19): 595-600.

Schumacher J.C., (1997), Appendix 2. The estimation of the proportion of ferric iron in the electron-microprobe analysis of amphiboles, in Leake et al.(1997), *The Canadian Mineralogist*, 35: 238-246.

Szymczak P. and Ladd A.J.C., (2014), Reactive-infiltration instabilities in rocks. Part 2. Dissolution of a porous matrix, *Journal of Fluid Mechanics*, 738: 591-630.

Sekine T., Katsura T. and Aramaki S., (1979), Water saturated phase relations of some andesites with application to the estimation of the initial temperature and water pressure at the time of eruption, *Geochimica et Cosmochimica Acta*, 43: 1367-1376.

Sisson T.W. and Grove T.L., (1993), Temperatures and H_2O contents of low-MgO high-alumina basalts, *Contributions to Mineralogy and Petrology*, 113: 167-184.

Takahashi E., (1978), Petrologic Model of the Crust and Upper Mantle of the Japanese Island Arcs, *Bulletin Volcanologique*, 41(4): 529-547.

Tollan P.M.E., O'Neill H.St.C., Hermann J., Benedictus A. and Arculus R.J., (2015), Frozen melt-rock reaction in a peridotite xenolith from arub-arc mantle recorded by diffusion of trace elements and water in olivine, *Earth and Planetary Science Letters*, 422: 169-181.

Turner S., Caulfield J., Turner M., van Keken P., Maury R., Sandiford M. and Prouteau G., (2012), Recent contribution of sediments and fluids to the mantle's volatile budget, Letters, *Nature Geoscience*, 5: 50-54

Vidal P., Dupuy C., Maury R. and Richard M., (1989), Mantle metasomatism above subduction zones: Trace-element and radiogenic isotope characteristics of peridotite xenoliths from Batan Island (Philippines), *Geology*, 17: 1115-1118.

Wassmann S. and Stöckhert B., (2013), Rheology of the plate interface – Dissolution precipitation creep in high pressure metamorphic rocks, *Tectonophysics*, 608: 1-29.

Wells P.R.A., (1977), Pyroxene thermometry in simple and complex systems, *Contributions to Mineralogy and Petrology*, 62: 129-139.

Wood B.J. and Banno S., (1973), Garnet-orthopyroxene and orthopyroxene-clinopyroxene relationships in simple and complex systems, *Contributions to Mineralogy and Petrology*, 42: 109-124.

Yang T.F., Lee T., Chen C.H., Cheng S.N., Knittel U., Punongbayan R.S. and Rasdas A.R., (1996), A double island arc between Taiwan and Luzon: consequence of ridge subduction, *Tectonophysics*, 258: 85-101.

Appendix 1

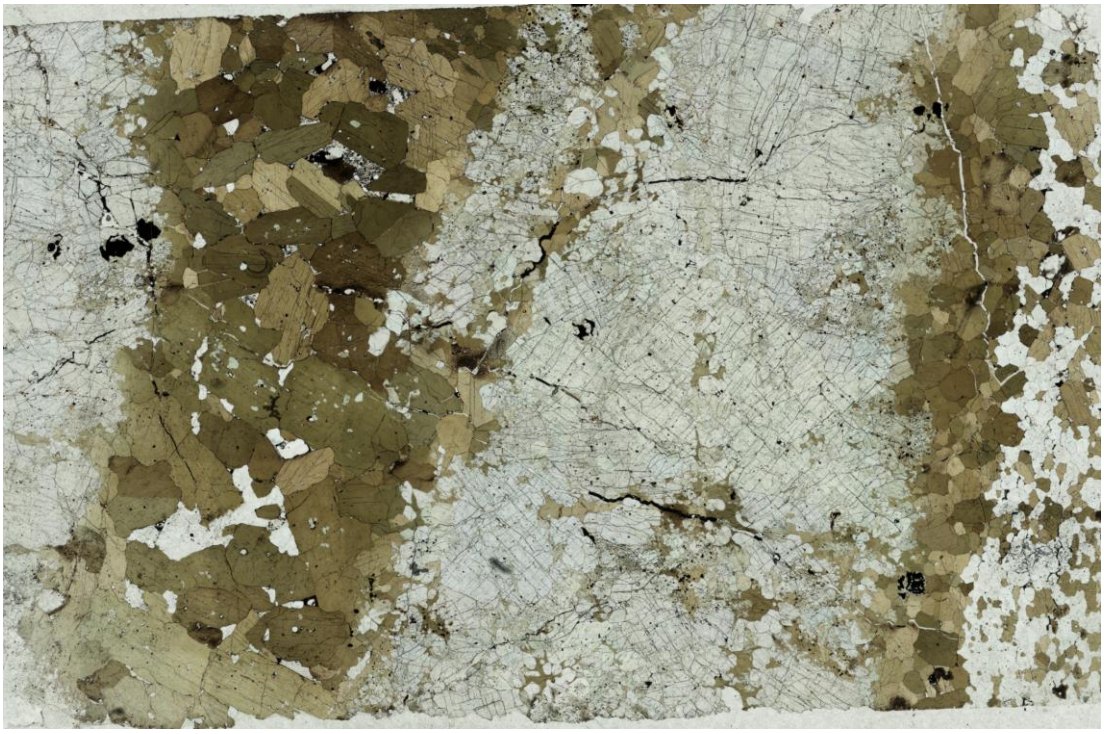

Figure 1. Thin section photo of the composite xenolith.

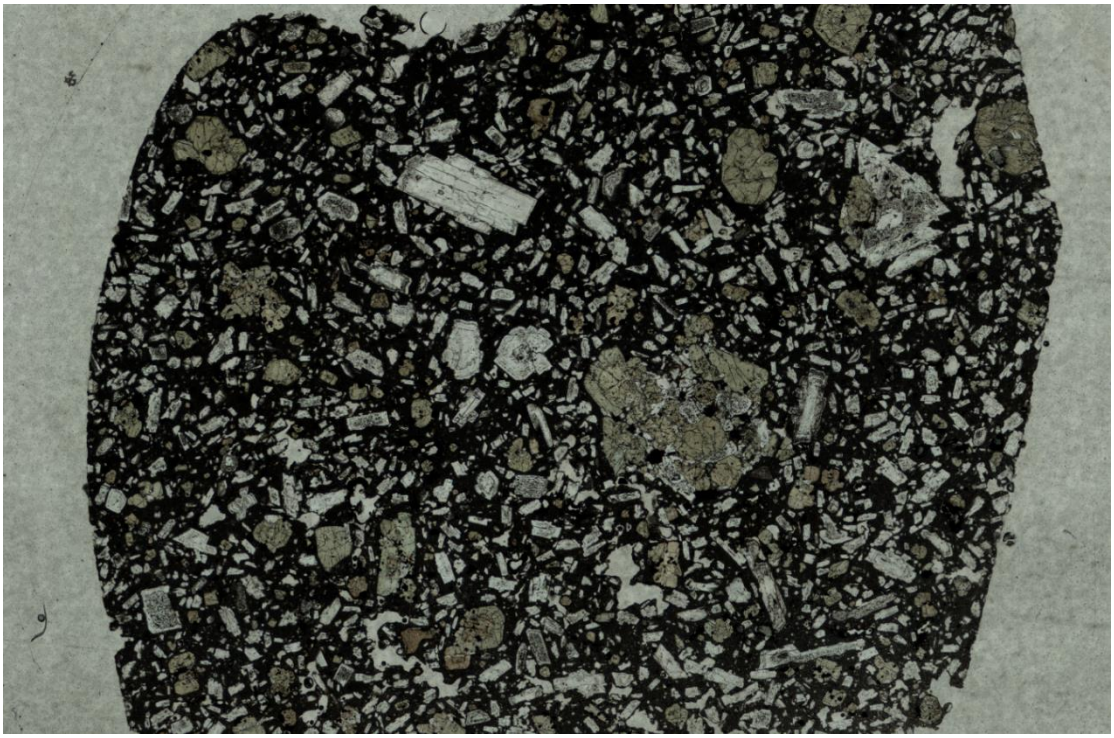

Figure 2: Thin section photo of the host andesite.

Appendix 2

Table 1- Hornblende

		Hornblendite								Hornblende Gabbro			Peridotite	
		Core-Rim												
		Horn-ite_amph_1	Horn-ite_amph_2	Horn-ite_amph_3	Horn-ite_amph_4	Horn-ite_amp_5	SH_amph_1	SH_amph_1	SH_amph_2	G_amph-plag_1	G_amph-plag_1	G_amph-plag_1	3 / 1 .	14 / 1 .
	SiO_2	40.82	41.99	40.68	40.68	40.88	41.55	40.73	40.22	40.53	40.86	40.84	41.66	42.50
	TiO_2	1.97	1.98	2.00	2.04	1.85	1.93	1.95	2.12	2.2	2.1	2.09	1.71	1.52
	Al_2O_3	13.65	13.19	13.48	13.98	13.26	13.38	13.90	13.57	13.52	13.78	13.59	13.70	13.15
	Cr_2O_3				0.06		0.10		0.05				0.03	0.59
	Fe_2O_3	**6.18**	**3.77**	**5.88**	**5.44**	**5.88**	**3.42**	**3.89**	**5.87**	**5.47**	**5.17**	**5.41**	**3.42**	**2.45**
	FeO	**5.57**	**6.74**	**5.03**	**5.52**	**4.73**	**6.85**	**7.51**	**5.96**	**6.27**	**6.62**	**6.30**	**6.28**	**6.88**
	MnO	0.14	0.12	0.15	0.13	0.13	0.10	0.15	0.16	0.14	0.11	0.14	0.12	0.14
	NiO				0.06	0.08							0.07	0.08
	MgO	15.11	15.69	15.58	15.28	16.00	15.26	14.46	14.83	14.96	14.93	15.22	15.52	15.70
	CaO	12.38	12.30	12.40	12.46	12.36	12.20	12.21	12.37	12.4	12.42	12.3	12.41	12.21
	Na_2O	2.36	2.38	2.25	2.24	2.47	2.38	2.32	2.12	2.14	2.2	2.26	2.37	2.40
	K_2O	0.97	0.91	0.92	0.99	0.83	0.90	0.93	1.1	1.17	1.1	1.07	0.94	0.82
	Total	99.15	99.08	98.37	98.88	98.47	98.07	98.05	98.37	98.80	99.29	99.22	98.23	98.43
	M	**82.9**	**80.6**	**84.7**	**83.1**	**85.8**	**79.9**	**77.4**	**81.60**	**80.97**	**80.09**	**81.15**	**81.50**	**80.27**
	Mg#	**70.8**	**73.4**	**72.9**	**72.3**	**74.0**	**73.3**	**70.1**	**70.16**	**70.44**	**70.24**	**70.83**	**74.72**	**75.48**
	Fe+3/Fe total	**0.5**	**0.335**	**0.513**	**0.47**	**0.528**	**0.31**	**0.318**	**0.47**	**0.44**	**0.413**	**0.436**	**0.329**	**0.243**
	no. of oxygens	**23**	**23**	**23**	**23**	**23**	**23**	**23**	**23**	**23**	**23**	**23**	**23**	**23**
T site	Si	5.898	6.046	5.905	5.882	5.922	6.042	5.957	5.872	5.892	5.907	5.904	6.036	6.137
	^{iv}Al	2.102	1.954	2.095	2.118	2.078	1.958	2.043	2.128	2.108	2.093	2.096	1.964	1.863
	∑ T site	8.000	8.000	8.000	8.000	8.000	8.000	8.000	8.000	8.000	8.000	8.000	8.000	8.000
M1-3 sites	Ti	0.214	0.214	0.218	0.222	0.202	0.211	0.215	0.233	0.241	0.228	0.227	0.187	0.165
	^{vi}Al	0.223	0.285	0.212	0.265	0.187	0.336	0.354	0.207	0.209	0.255	0.221	0.376	0.377
	Cr	0.000	0.000	0.000	0.007	0.000	0.011	0.000	0.006	0.000	0.000	0.000	0.004	0.067
	Fe^{+3}	0.672	0.409	0.643	0.592	0.641	0.374	0.428	0.645	0.599	0.563	0.589	0.373	0.267
	Fe^{+2}	0.666	0.795	0.602	0.659	0.564	0.818	0.903	0.719	0.752	0.787	0.747	0.750	0.812
	Ni	0.000	0.000	0.000	0.007	0.009	0.000	0.000	0.000	0.000	0.000	0.000	0.008	0.010
	Mg	3.224	3.296	3.325	3.248	3.398	3.248	3.100	3.190	3.200	3.167	3.216	3.302	3.303
	∑ M1-3 sites	5.000	5.000	5.000	5.000	5.000	5.000	5.000	5.000	5.000	5.000	5.000	5.000	5.000
M4 sites	Fe^{+2}	0.006	0.017	0.008	0.009	0.009	0.015	0.015	0.008	0.010	0.012	0.015	0.011	0.019
	Mn	0.017	0.015	0.018	0.016	0.016	0.012	0.019	0.020	0.017	0.013	0.017	0.015	0.017
	Mg	0.029	0.070	0.045	0.044	0.056	0.059	0.052	0.037	0.041	0.050	0.063	0.048	0.075
	Ca	1.917	1.898	1.929	1.930	1.919	1.901	1.914	1.935	1.931	1.924	1.905	1.926	1.889
	Na	0.031	0.000	0.000	0.000	0.000	0.013	0.000	0.000	0.000	0.000	0.000	0.000	0.000
	∑ M4 site	2.000	2.000	2.000	2.000	2.000	2.000	2.000	2.000	2.000	2.000	2.000	2.000	2.000
A site	Na	0.630	0.664	0.633	0.628	0.694	0.659	0.658	0.600	0.603	0.616	0.634	0.665	0.671
	K	0.179	0.167	0.170	0.183	0.153	0.167	0.174	0.205	0.217	0.203	0.197	0.173	0.151
	∑ A site	0.809	0.831	0.804	0.810	0.847	0.826	0.831	0.805	0.820	0.819	0.831	0.838	0.822
	∑ Cations	**15.809**	**15.831**	**15.804**	**15.810**	**15.847**	**15.826**	**15.831**	**15.805**	**15.820**	**15.819**	**15.831**	**15.838**	**15.822**

Table 5.1: Presenting major element abundances in weight percent oxides and chemical formula for representative analysis points. FeO is total Fe. b.d.l. – Below detection limits. Structural formula calculated using the process outlined in Deer et al. (1992). Fe^{2+} and Fe^{3+} calculated following Schumacher (1997) Mg# calculated from structural formula as Mg# = Mg*100/ (Mg + Fe), M number is calculated as M = Mg*100 / (Mg + Fe^{2+}).

Table 2- Olivine

	Olivine										
	1 / 1 .	2 / 1 .	4 / 1 .	5 / 1 .	6 / 1 .	11 / 1 .	12 / 1 .	32 / 1 .	33 / 1 .	44 / 1 .	45 / 1 .
SiO_2	39.38	39.47	39.95	40.13	39.33	40.17	40.26	38.87	39.10	39.61	39.43
TiO_2	b.d.l.	b.d.l.	b.d.l.	b.d.l.	0.00	0.01	0.00	0.00	0.00	0.02	0.01
Al_2O_3	0.03	0.02	0.02	0.02	0.00	0.00	0.02	0.01	b.d.l.	0.03	0.02
Cr_2O_3	b.d.l.	b.d.l.	b.d.l.	0.03	0.02	0.00	0.01	b.d.l.	0.00	0.03	0.01
Fe_2O_3	b.d.l.	b.d.l.	b.d.l.	b.d.l.	b.d.l.	b.d.l.	b.d.l.	b.d.l.	b.d.l.	b.d.l.	b.d.l.
FeO	18.42	18.71	18.20	17.24	17.27	18.79	18.47	19.51	19.41	17.48	17.38
MnO	0.41	0.41	0.40	0.38	0.39	0.39	0.40	0.44	0.42	0.38	0.38
NiO	0.26	0.27	0.24	0.25	0.30	0.24	0.24	0.27	0.21	0.27	0.26
MgO	41.76	41.49	41.60	42.79	43.03	41.21	41.80	41.24	41.14	43.01	43.39
CaO	0.12	0.13	0.12	0.13	0.12	0.16	0.13	0.13	0.12	0.08	0.10
Na_2O	0.02	b.d.l.	0.02	b.d.l.	0.03	b.d.l.	0.01	b.d.l.	b.d.l.	b.d.l.	b.d.l.
K_2O	b.d.l.	b.d.l.	b.d.l.	b.d.l.	b.d.l.	b.d.l.	b.d.l.	b.d.l.	b.d.l.	b.d.l.	b.d.l.
Total	100.40	100.50	100.56	100.99	100.48	100.99	101.33	100.48	100.40	100.91	100.98
Mg#	**80.16**	**79.81**	**80.29**	**81.56**	**81.62**	**79.63**	**80.13**	**79.02**	**79.06**	**81.43**	**81.65**
Oxygens	**4**	**4**	**4**	**4**	**4**	**4**	**4**	**4**	**4**	**4**	**4**
Si	1.002	1.005	1.012	1.008	0.996	1.016	1.013	0.995	1.000	0.998	0.994
Ti	0.000	0.000	0.000	0.000	0.000	0.000	0.000	0.000	0.000	0.000	0.000
Al	0.001	0.001	0.001	0.001	0.000	0.000	0.001	0.000	0.000	0.001	0.001
Cr	0.000	0.000	0.000	0.001	0.000	0.000	0.000	0.000	0.000	0.001	0.000
Fe+3	0.000	0.000	0.000	0.000	0.000	0.000	0.000	0.000	0.000	0.000	0.000
Fe+2	0.392	0.398	0.386	0.362	0.366	0.397	0.389	0.418	0.415	0.369	0.366
Mn	0.009	0.009	0.009	0.008	0.008	0.008	0.009	0.009	0.009	0.008	0.008
Ni	0.005	0.006	0.005	0.005	0.006	0.005	0.005	0.006	0.004	0.006	0.005
Mg	1.584	1.574	1.571	1.602	1.624	1.553	1.567	1.573	1.568	1.616	1.629
Ca	0.003	0.003	0.003	0.004	0.003	0.004	0.003	0.004	0.003	0.002	0.003
Na	0.001	0.000	0.001	0.000	0.001	0.000	0.000	0.000	0.000	0.000	0.000
∑ Cations	2.998	2.995	2.988	2.991	3.005	2.984	2.987	3.005	3.000	3.001	3.006

Table 2: Major element concentrations for Olivine. Abbreviations as in Table 1.

Table 3- Clinopyroxene and Orthopyroxene (XENOLITH)

		Clinopyroxene							Orthopyroxene		
		7 / 1 .	10 / 1 .	20 / 1 .	24 / 1 .	29 / 1 .	Peri_Mingroup_1	Peri_Mingroup_2	22 / 1 .	30 / 1 .	31 / 1 .
	SiO_2	52.18	52.13	51.38	52.74	53.68	50.65	52.14	56.44	56.46	56.87
	TiO_2	0.20	0.25	0.39	0.23	0.18	0.55	0.26	0.04	b.d.l.	0.04
	Al_2O_3	2.49	3.02	3.80	2.76	1.71	4.51	2.73	1.11	0.55	1.08
	Cr_2O_3	0.49	b.d.l.	0.03	0.44	0.08	b.d.l.	0.43	0.07	0.05	0.07
	Fe_2O_3	**0.48**	**2.69**	**2.96**	**1.91**	**1.78**	**3.83**	**2.98**	**0.00**	**1.13**	**0.00**
	FeO	**4.33**	**3.08**	**3.25**	**3.66**	**3.41**	**2.82**	**2.79**	**11.46**	**10.24**	**11.54**
	MnO	0.17	0.18	0.18	0.16	0.17	0.19	0.15	0.38	0.37	0.37
	NiO	0.02	0.06	0.02	0.04	0.09	0.00	0.00	0.05	0.07	0.09
	MgO	15.85	15.96	15.43	16.00	16.84	15.02	15.96	30.28	31.31	30.41
	CaO	22.70	23.26	23.26	23.07	23.03	23.41	23.38	1.18	0.78	1.20
	Na_2O	0.26	0.22	0.23	0.29	0.26	0.28	0.26	0.01	0.01	0.02
	K_2O	0.01	0.01	0.00	0.00	0.01	0.00	0.00	b.d.l.	b.d.l.	b.d.l.
	Total	99.17	100.85	100.92	101.28	101.24	101.27	101.08	101.03	100.95	101.68
	M	**86.70**	**90.22**	**89.42**	**88.63**	**89.80**	**90.46**	**91.07**	**82.48**	**84.49**	**82.45**
	$Mg^{\#}$	**85.58**	**83.79**	**82.30**	**84.14**	**85.69**	**81.02**	**83.87**	**82.48**	**83.22**	**82.45**
	Fe+3/Fe total	**0.09**	**0.44**	**0.45**	**0.32**	**0.32**	**0.55**	**0.49**	**0**	**0.09**	**0**
	no. of oxygens	**6**	**6**	**6**	**6**	**6**	**6**	**6**	**6**	**6**	**6**
T sites	Si	1.931	1.899	1.874	1.913	1.942	1.845	1.897	1.976	1.974	1.979
	^{iv}Al	0.069	0.101	0.126	0.087	0.058	0.155	0.103	0.024	0.026	0.021
	∑ T site	2.000	2.000	2.000	2.000	2.000	2.000	2.000	2.000	2.000	2.000
M1 sites	Ti	0.006	0.007	0.011	0.006	0.005	0.015	0.007	0.001	0.000	0.001
	^{vi}Al	0.039	0.028	0.038	0.031	0.015	0.039	0.014	0.022	-0.004	0.023
	Cr	0.014	0.000	0.001	0.013	0.002	0.000	0.012	0.002	0.001	0.002
	Fe^{+3}	0.013	0.074	0.081	0.052	0.049	0.105	0.082	0.000	0.030	0.000
	Fe^{+2}	0.134	0.087	0.092	0.102	0.094	0.080	0.079	0.171	0.151	0.171
	Ni	0.001	0.002	0.001	0.001	0.003	0.000	0.000	0.001	0.002	0.002
	Mg	0.793	0.802	0.777	0.795	0.832	0.761	0.806	0.803	0.820	0.801
	∑ M1 site	1.000	1.000	1.000	1.000	1.000	1.000	1.000	1.000	1.000	1.000
M2 sites	Mg	0.081	0.064	0.062	0.069	0.076	0.05	0.06	0.78	0.81	0.78
	Fe^{+2}	0.000	0.007	0.007	0.009	0.009	0.006	0.006	0.165	0.149	0.165
	Mn	0.005	0.005	0.006	0.005	0.005	0.006	0.005	0.011	0.011	0.011
	Ca	0.900	0.908	0.909	0.896	0.893	0.914	0.911	0.044	0.029	0.045
	Na	0.019	0.016	0.016	0.020	0.018	0.020	0.018	0.001	0.001	0.002
	∑ M2 site	1.005	1.000	1.000	1.000	1.000	1.000	1.000	0.999	1.000	0.998
	∑ Cations	4.005	4.000	4.000	4.000	4.000	4.000	4.000	3.999	4.000	3.998

Table 3: Major element concentrations as structural formula for clinopyroxene and orthopyroxene for the xenolith. Abbreviations as in Table 1.

Table 4- Clinopyroxene and Orthopyroxene (HOST ANDESITE)

		Host_pyx_group_	lost_pyx_group_	lost_pyx_group_	lost_pyx_group_	lost_pyx_group_	lost_pyx_group_
	Position		rim	core			
	Mineral	CPX	CPX	OPX	CPX	CPX	CPX
	SiO_2	50.56	50.39	54.02	51.21	52.35	51.17
	TiO_2	0.49	0.48	0.26	0.48	0.41	0.59
	Al_2O_3	2.60	3.79	1.58	2.61	2.41	2.46
	Cr_2O_3	0.00	0.07	0.00	0.00	0.00	0.00
	Fe_2O_3	**3.12**	**3.80**	**0.20**	**2.94**	**1.67**	**2.73**
	FeO	**9.40**	**4.53**	**17.51**	**7.94**	**7.33**	**9.23**
	MnO	0.38	0.19	0.48	0.33	0.28	0.40
	NiO	0.00	0.00	0.00	0.00	0.00	0.00
	MgO	14.43	15.69	24.92	15.21	15.45	14.65
	CaO	18.62	21.03	1.89	19.40	20.78	19.21
	Na_2O	0.34	0.22	0.00	0.30	0.25	0.29
	K_2O	0.00	0.00	0.00	0.00	0.00	0.00
	Total	99.94	100.19	100.86	100.42	100.93	100.72
	M	**73.23**	**86.05**	**71.72**	**77.34**	**78.98**	**73.89**
	Mg#	**67.80**	**77.86**	**71.51**	**71.91**	**75.72**	**69.09**
	Fe+3/Fe total	**0.23**	**0.43**	**0.01**	**0.25**	**0.17**	**0.21**
	no. of oxygens	**6**	**6**	**6**	**6**	**6**	**6**
T sites	Si	1.897	1.859	1.956	1.900	1.923	1.902
	^{iv}Al	0.103	0.141	0.044	0.100	0.077	0.098
	∑ T site	2.000	2.000	2.000	2.000	2.000	2.000
M1 sites	Ti	0.014	0.013	0.007	0.013	0.011	0.016
	^{vi}Al	0.012	0.024	0.024	0.014	0.027	0.010
	Cr	0.000	0.002	0.000	0.000	0.000	0.000
	Fe^{+3}	0.088	0.105	0.005	0.082	0.046	0.076
	Fe^{+2}	0.285	0.189	0.275	0.250	0.222	0.277
	Ni	0.000	0.000	0.000	0.000	0.000	0.000
	Mg	0.601	0.666	0.689	0.640	0.693	0.620
	∑ M1 site	1.000	1.000	1.000	1.000	1.000	1.000
M2 sites	Mg	0.206	0.196	0.656	0.200	0.153	0.192
	Fe^{+2}	0.010	-0.050	0.256	-0.004	0.003	0.009
	Mn	0.012	0.006	0.015	0.010	0.009	0.013
	Ca	0.748	0.831	0.073	0.771	0.818	0.765
	Na	0.025	0.016	0.000	0.022	0.018	0.021
	∑ M2 site	1.000	1.000	1.000	1.000	1.000	1.000
	∑ Cations	4.000	4.000	4.000	4.000	4.000	4.000

Table 4: Major element concentrations and structural formula for clinopyroxene (CPX) and orthopyroxene (OPX) within the host andesite. Abbreviations as in Table 1.

Table 5- Plagioclase (XENOLITH and HOST ANDESITE)

	Xenolith						Host Andesite		
	Horn-ite_plag_1	Horn-ite_plag_2	Horn-ite_plag_3	Horn-ite_plag_4	HG_amph-plag_2	HG_amph-plag_3	phenocrysts	phenocrysts	phenocrysts
SiO_2	44.50	44.32	44.02	44.69	44.16	44.42	48.21	46.23	50.34
TiO_2	b.d.l.	b.d.l.	b.d.l.	b.d.l.	b.d.l.	b.d.l.	b.d.l.	b.d.l.	b.d.l.
Al_2O_3	34.40	34.79	34.29	34.79	34.93	34.96	32.57	33.55	30.64
Cr_2O_3	b.d.l.	b.d.l.	b.d.l.	b.d.l.	b.d.l.	b.d.l.	b.d.l.	b.d.l.	b.d.l.
FeO	0.57	0.49	0.57	0.58	0.71	0.64	0.75	0.73	0.77
MnO	b.d.l.	b.d.l.	b.d.l.	b.d.l.	b.d.l.	b.d.l.	b.d.l.	b.d.l.	b.d.l.
MgO	0.03	b.d.l.	b.d.l.	0.04	0.04	0.03	0.06	0.04	0.06
CaO	19.10	19.29	19.18	19.00	19.41	19.13	16.55	17.97	14.8
Na_2O	0.76	0.68	0.74	0.86	0.70	0.69	2.39	1.43	3.3
K_2O	0.03	0.04	b.d.l.	0.03	b.d.l.	b.d.l.	0.08	0.04	0.14
Total	99.39	99.61	98.80	99.99	99.95	99.87	100.61	99.99	100.05
# oxygens	**32**	**32**	**32**	**32**	**32**	**32**	**32**	**32**	**32**
Si	8.300	8.249	8.266	8.283	8.205	8.245	8.824	8.545	9.219
Ti	0.000	0.000	0.000	0.000	0.000	0.000	0.000	0.000	0.000
Al	7.564	7.634	7.591	7.602	7.652	7.650	7.028	7.311	6.615
Cr	0.000	0.000	0.000	0.000	0.000	0.000	0.000	0.000	0.000
Fe+2	0.089	0.076	0.090	0.090	0.110	0.099	0.115	0.113	0.118
Mn	0.000	0.000	0.000	0.000	0.000	0.000	0.000	0.000	0.000
Mg	0.008	0.000	0.000	0.011	0.011	0.008	0.016	0.011	0.016
Ca	3.817	3.847	3.859	3.773	3.864	3.804	3.246	3.559	2.904
Na	0.275	0.245	0.269	0.309	0.252	0.248	0.848	0.512	1.172
K	0.007	0.009	0.000	0.007	0.000	0.000	0.019	0.009	0.033
∑ Cations	**20.060**	**20.061**	**20.074**	**20.075**	**20.095**	**20.055**	**20.096**	**20.061**	**20.076**
An#	**93.3**	**94.0**	**93.5**	**92.4**	**93.9**	**93.9**	**79.3**	**87.4**	**71.3**
Ca	93.1	93.8	93.5	92.3	93.9	93.9	78.9	87.2	70.7
Na	6.7	6.0	6.5	7.6	6.1	6.1	20.6	12.6	28.5
K	0.2	0.2	0.0	0.2	0.0	0.0	0.5	0.2	0.8

Table 5.5: Major element abundances for plagioclase in both xenolith and host andesite. Structural formula calculated as from Deer et al. (1992), An# is Ca*100/ (Na+K). Ca = Ca*100 / (Ca+Na+K), Na = Na *100 / (Ca+Na+K), K = K*100 / (Ca+Na+K). other abbreviations as in Table 1..

TABLE 6- Glass phases

		Host Andesite	Ol. melt inclusions	
	SiO_2	**58.53**	**63.74**	**64.06**
	TiO_2	0.22	0.25	0.30
	Al_2O_3	20.29	19.22	18.88
	Cr_2O_3	b.d.l.	b.d.l.	b.d.l.
	FeO(total)	4.02	3.03	2.92
	MnO	0.12	b.d.l.	b.d.l.
	NiO	b.d.l.	b.d.l.	b.d.l.
	MgO	2.32	1.56	1.08
	CaO	8.37	4.01	4.24
	Na_2O	4.83	5.32	5.65
	K_2O	1.15	3.91	3.96
	Total	99.85	101.04	101.09
	Na_2O+K_2O	**5.98**	**9.23**	**9.61**
	Mg#	50.70	47.85	39.73
CMAS	Qtz	44.34	45.10	45.12
CMAS	$CaAl_2O_4$	49.91	49.94	51.72
CMAS	Fo	5.75	4.96	3.17
CMAS	Total	100.00	100.00	100.00

Table 6: Major element abundances for glass phases as melt inclusions in olivine (within the xenolith) and the host andesite matrix. CMAS calculations as those in Adam et al. (2016b).

Appendix 3

Table 5.1

	Peridotite fragment						Hornblendite				Hornblende Gabbro				
Element	ol BIX-ol-03	ol BIX-ol-p1-14	ol BIX-ol-p3-27	cpx BIX-cpx-01	cpx BIX-cpx-17	opx BIX-opx-02	hbl BIX-hbl-07	hbl BIX-hbl-p1-08	hbl BIX-hbl-p1-11	feld BIX-pl-05	hbl BIX-hbl-19	hbl BIX-hbl-24	feld BIX-pl-p2-23	feld BIX-pl-25	D.L.
Li	3.22	2.7	3.24	1.67	1.23	1.3	1.3	0.98	1.26	1.06	1.02	1.18	0.82	0.48	0.2950
K	678.89	9.42	b.d.l.	b.d.l.	b.d.l.	b.d.l.	8980.72	8255.74	8278.27	272.86	9023.83	9347.46	281.02	852.09	1.773
Ca	1037.32	884.47	879.92	153835.94	161234.31	6431.92	83392.56	83319.23	80867.78	117667	83490.56	84189.89	126166.34	122519.62	20.75
Ti	34.13	28.78	28.9	654.73	1287.09	263.7	11287.43	11633.19	9536.02	46.17	11891.62	12044.85	54.3	180.09	0.3676
V	2.92	2.216	2.375	182.46	122.96	34.25	500.03	555.71	448.77	0.634	565.74	572.27	0.882	7.98	0.0374
Co	146.02	177.42	171.39	24.5	27.24	61.09	50.58	52.88	48.06	0.221	54.55	56.02	0.297	0.827	0.01712
Rb	4.85	b.d.l.	b.d.l.	0.079	b.d.l.	b.d.l.	9.44	6.36	8.07	b.d.l.	7.08	7.37	0.253	3.43	0.05594
Sr	9.33	0.0125	b.d.l.	49.81	48.62	0.123	393.66	333.01	317.11	927.83	317.27	362.17	1074.71	1135.88	2.705
Y	0.156	0.072	0.0475	10.95	10.68	0.824	17.71	20.91	17.74	0.075	21.15	16.92	0.093	0.547	0.01032
Zr	2.168	0.037	b.d.l.	18.32	19.56	0.642	50.47	49.26	51.15	0.042	64.29	39.11	0.192	4.77	0.01971
Nb	0.0711	b.d.l.	b.d.l.	0.0219	0.0203	b.d.l.	3.25	3.81	3.33	b.d.l.	4.89	2.29	b.d.l.	0.322	0.00884
Ba	14.03	b.d.l.	b.d.l.	0.137	0.0598	b.d.l.	253.4	167.32	239.06	46.24	207.31	266.26	54.64	69.92	0.01384
La	0.374	b.d.l.	b.d.l.	2.001	2.277	b.d.l.	4.63	4.3	5.51	1.68	5.79	5.03	1.904	2.91	0.00902
Ce	0.723	b.d.l.	b.d.l.	9.01	9.78	0.0304	17.35	17.85	20.86	2.71	23.21	18.28	3.38	5.47	0.00642
Pr	0.079	b.d.l.	b.d.l.	1.942	1.978	b.d.l.	3.21	3.54	3.89	0.291	4.37	3.13	0.345	0.613	0.00607
Nd	0.325	b.d.l.	b.d.l.	12	11.12	0.088	18.02	21.25	20.6	1.29	25.08	16.61	1.217	1.88	0.03833
Sm	0.07	b.d.l.	b.d.l.	3.2	2.94	0.053	4.96	5.59	4.96	0.132	5.99	4.42	0.112	0.355	0.04840
Eu	b.d.l.	b.d.l.	b.d.l.	0.738	0.78	0.0139	1.383	1.483	1.459	0.23	1.587	1.4	0.267	0.286	0.01276
Gd	0.055	b.d.l.	b.d.l.	2.64	2.15	0.094	4.18	4.81	3.96	b.d.l.	4.92	3.76	b.d.l.	0.142	0.05211
Tb	0.0066	b.d.l.	b.d.l.	0.354	0.346	0.0156	0.599	0.671	0.562	b.d.l.	0.703	0.537	0.0084	0.0165	0.00614
Dy	0.032	0.0155	b.d.l.	2.3	1.978	0.121	3.74	4.37	3.66	b.d.l.	4.2	3.25	0.047	0.11	0.02604
Ho	0.0101	b.d.l.	b.d.l.	0.427	0.416	0.0408	0.737	0.862	0.685	0.0092	0.884	0.704	b.d.l.	0.0229	0.00686
Er	b.d.l.	b.d.l.	b.d.l.	1.183	1.246	0.129	1.817	2.153	1.801	0.0262	2.42	1.79	b.d.l.	0.043	0.02255
Tm	b.d.l.	b.d.l.	b.d.l.	0.165	0.179	0.0283	0.241	0.29	0.253	b.d.l.	0.308	0.229	b.d.l.	b.d.l.	0.00668
Yb	b.d.l.	b.d.l.	0.0385	0.93	1.078	0.161	1.488	1.828	1.728	b.d.l.	1.97	1.479	0.038	b.d.l.	0.03096
Lu	0.0079	0.0111	0.0091	0.133	0.155	0.0192	0.228	0.243	0.209	b.d.l.	0.269	0.206	b.d.l.	0.0162	0.00710
Hf	0.055	b.d.l.	b.d.l.	1.422	1.234	0.038	2.098	2.15	2.057	b.d.l.	2.82	1.539	b.d.l.	0.103	0.02388
Ta	b.d.l.	b.d.l.	b.d.l.	b.d.l.	b.d.l.	b.d.l.	0.1402	0.1735	0.1392	b.d.l.	0.248	0.0967	b.d.l.	0.0087	0.00589
Pb	0.614	b.d.l.	0.057	0.12	0.083	b.d.l.	1.618	1.012	1.099	1.191	1.193	1.425	1.29	1.465	0.02836
Th	0.411	0.0088	b.d.l.	0.0789	0.158	b.d.l.	0.577	0.224	0.411	b.d.l.	0.23	0.322	0.0297	0.53	0.00733
U	0.0514	b.d.l.	b.d.l.	0.01	0.0192	b.d.l.	0.1093	0.0265	0.0496	b.d.l.	0.0465	0.0374	b.d.l.	0.112	0.00805

Table 5.1: Trace element abundances from Li to U in ppm of representative point analyses. ol- Olivine. cpx- Clinopyroxene. opx- Orthopyroxene. hbl- Hornblende. feld- Feldspar.

b.d.l..- detection limits calculated as an average D.L. for each element. b.d.l.- Below detection limits